Title: Structure of human PINK1 at a mitochondrial TOM-VDAC array

Authors: Sylvie Callegari[1,2*], Nicholas S Kirk[1,2], Zhong Yan Gan[1,2], Toby Dite[1,2], Simon A Cobbold[1,2], Andrew Leis[1,2], Laura F Dagley[1,2], Alisa Glukhova[1,2,3,4,5*] and David Komander[1,2*]

Affiliations:

[1] Walter and Eliza Hall Institute of Medical Research, Parkville, Victoria, Australia

[2] Department of Medical Biology, University of Melbourne, Melbourne, Victoria, Australia

[3] Department of Biochemistry and Pharmacology, The University of Melbourne, Melbourne, Victoria 3010, Australia

[4] Drug Discovery Biology, Monash Institute of Pharmaceutical Sciences, Monash University, 381 Royal Parade, Parkville 3052, Victoria Australia

[5]ARC Centre for Cryo-electron Microscopy of Membrane Proteins, Monash Institute of Pharmaceutical Sciences, Monash University, 381 Royal Parade, Parkville 3052, Victoria Australia

*Corresponding authors. Email: callegari.s@wehi.edu.au, glukhova.a@wehi.edu.au, dk@wehi.edu.au

Abstract:

Mutations in the ubiquitin kinase PINK1 cause early onset Parkinson's Disease, but how PINK1 is stabilized at depolarized mitochondrial translocase complexes has remained poorly understood. We determined a 3.1-Å resolution cryo-electron microscopy structure of dimeric human PINK1 stabilized at an endogenous array of mitochondrial TOM and VDAC complexes. Symmetric arrangement of two TOM core complexes around a central VDAC2 dimer is facilitated by TOM5 and TOM20, both of which also bind PINK1 kinase C-lobes. PINK1 enters mitochondria through the proximal TOM40 barrel of the TOM core complex, guided by TOM7 and TOM22. Our structure explains how human PINK1 is stabilized at the TOM complex and regulated by oxidation, uncovers a previously unknown TOM-VDAC assembly, and reveals how a physiological substrate traverses TOM40 during translocation.

Main Text:

Mutations in the protein kinase PARK6/PINK1 lead to early-onset forms of Parkinson's Disease (EOPD) (*1*). PINK1 is a ubiquitin and Parkin kinase (*2–7*) and functions as an early sensor and transducer of mitochondrial damage signaling (*8–10*). In healthy mitochondria, PINK1 is translocated across the mitochondrial outer membrane (MOM) via the translocase of the outer membrane (TOM) complex, inserted into the mitochondrial inner membrane (MIM) via the translocase of the inner membrane (TIM)23 complex, cleaved by the MIM protease PARL, retro-translocated and degraded by the proteasome (*10*). Depolarization leads to stalled import into the inner membrane and PINK1 is stabilized at the MOM, where the kinase domain becomes activated, and triggers mitophagy by generating phospho-ubiquitin (pUb) to recruit and initiate activation of the E3 ubiquitin ligase Parkin. Full activation of Parkin by PINK1 phosphorylation unleashes its E3 ligase activity and leads to ubiquitination of many MOM proteins (*11–14*). The assembled carpet of short-chain ubiquitin and pUb signals (*15–18*) initiates mitophagy of the damaged mitochondrion.

Multiple structures of isolated kinase domains of PINK1 from insects have provided molecular details about PINK1 activation (*19–21*), which has been biochemically confirmed in human PINK1 (*3*, *12*, *21*, *22*). However, human PINK1 has resisted structural characterization, and the PINK1 N-terminus (1-115) which comprises many patient mutations (*23*) has remained unresolved. A structure of full-length PINK1 at mitochondria is crucial to develop and understand PINK1 activators and treat Parkinson's disease (*24–26*).

Mechanisms of mitochondrial protein import have been intensely studied over the last 5 decades, yet many questions remain (*27–30*). The TOM complex is the main entry gate for all ~1500 proteins that are imported into mitochondria as unfolded precursors. Yet how these precursors pass through the TOM complex after recognition by the presequence receptors TOM20 and TOM22 has not been resolved, nor has it been established how mitochondrial presequence-containing precursors are handed over from the TOM to the TIM23 complex (*30*). PINK1 is stabilized on the outer mitochondrial membrane after depolarization, but how and why is unclear (*10*). A ~700 kDa PINK1-TOM complex was reported in 2012 (*31*, *32*), and TOM7 (*33*), TOM20 (*34*, *35*), and more recently the TIM23 complex (*36*, *37*), were shown to be functionally important in PINK1 stabilization.

We here report the structure of human PINK1 arrested after depolarization, at an endogenous mitochondrial import array comprising TOM and VDAC2 channels. The structure explains how PINK1 interacts with five TOM complex components, VDAC2, and phospholipids, unveils how a physiological presequence import substrate traverses the MOM, and rationalizes EOPD patient mutations. The structural role for VDAC channels in forming mitochondrial import arrays may illuminate how mitophagy is initiated.

Characterization of stabilized PINK1 on human mitochondria

To understand human PINK1 stabilization, we studied PINK1 in its endogenous environment on depolarized mitochondria. We realized that an unknown 100 kDa band arising from hydrogen peroxide treatment in our earlier work (*21*), was indeed an adduct between Cys40 of PINK1 and TIM50 (**fig. S1**). This observation indicated that PINK1 could be used to trap a TOM-TIM23 supercomplex, as has since been reported (*36*, *37*).

For biochemical and structural studies, we exploited a scalable Expi293™ human cell expression system, in which we expressed 3xFLAG-tagged wild-type human PINK1. Stabilization of PINK1 by oligomycin/antimycin A (OA) treatment for 3 hours was followed by mitochondrial isolation, membrane solubilization in digitonin, PINK1 immunoprecipitation, and a final size exclusion chromatography (SEC) step that resulted in a single peak (**Fig. 1A**, **fig. S2A**). Fractions within the peak were comprised of a 750 kDa complex as measured by mass-photometry (**Fig. 1A, fig. S2B**), which was further characterized by Western blotting (**Fig. 1B**), activity assays (**fig. S2C**) and mass spectrometry (MS) (**Fig. 1C, data S1**). Chemical cross-linking MS (XL-MS) analysis of the purified complex mapped 250+ intraprotein crosslinks and 35+ crosslinks between complex components (**data S2**). A network of crosslinks was observed between PINK1 and TOM components, including TOM7, TOM40 and TOM20. The N-terminus of PINK1 formed crosslinks with TIM50 and TIM17B, and further intriguing crosslinks were detected between TOM40 and the inter-membrane space (IMS) domain of TIM50, corroborating the notion of a stabilized TOM-TIM23 supercomplex (**fig. S3, table S1**). MS analysis of purified complex components also identified mitochondrial proteins not initially expected to be part of a PINK1-TOM-TIM23 supercomplex, including mitochondrial voltage-dependent anion channels (VDAC1, VDAC2 and VDAC3), acylglycerol kinase (AGK), and chaperones (Hsp90, mtHsp60, mtHsp70) (**Fig. 1C, data S1**).

Large scale purification from Expi293™ cells, generated a complex in detergent micelles at sufficient concentration (4 mg/ml) to perform cryo-electron microscopy (cryo-EM) single particle analysis. Immediately apparent within the 2D classes were large, regular protein assemblies. The dominant species present was revealed to be an oval-shaped disc with six pores (**fig. S4A**). High-resolution 3D reconstruction resulted in a cryoEM map with a global resolution of 3.1 Å (local resolution range; 2-13 Å) (**Fig. 1D, E**). Further symmetry expansion and local refinement resolved one half of the complex with a global resolution of 2.7 Å (local resolution; 2-6 Å). The trans-membrane domain of TOM20 was also resolved using 3D variability and local refinement to 3.3 Å (local resolution; 2-13 Å) (**fig. S4B**).

The complete complex reconstruction (**Fig. 1D-F**) includes two TOM core complexes, each comprising of two copies of TOM40, TOM7, TOM6, TOM5 and TOM22, and one copy of TOM20 (*29*). The two TOM core complexes are arranged symmetrically around a central VDAC2 dimer, connected by TOM5. Human PINK1 kinase domains form a symmetric dimer as in previous insect structures (*20*, *21*), that sits atop the VDAC dimer, and is held in position by interactions with TOM5, and extensive contacts with TOM20 which forms a helical brace for the PINK1 kinase dimer. The PINK1 N-termini are threaded into the barrel of the VDAC-proximal TOM40 channels and exit into the IMS guided by TOM7 and TOM22 **(Fig. 1D-F)**. The high-resolution structure also resolves 18 lipid molecules, some of which contact PINK1 (**fig. S5**).

The TOM – VDAC array

An assembly of TOM and VDAC complexes (**Fig. 2A**) has not previously been reported and provides insights into arrangements of endogenous mitochondrial outer membrane (MOM) complexes. Individually, the two TOM core complexes are similar to previous structures of the human TOM complex (*38–41*) (**fig. S6**), including the location of lipid molecules (**fig. S5, S6B**). For a comparison of our TOM complex structure with published TOM structures across species, see **fig. S6**. Our larger structure reveals new roles for TOM5 and illuminates TOM20-TOM22

interactions. This complex structure additionally provides a high resolution reconstruction of human VDAC2, a VDAC channel with specific roles in apoptosis (*42*, *43*) (**Fig. 2B**). The rationale for modelling a VDAC2 dimer is explained in Supplementary Text and depicted in **fig. S7**.

VDAC dimers and oligomers can form through a variety of interfaces (*44*). Our VDAC2 dimer forms through symmetric interactions of β-sheets 1 to 6 which on the IMS side juxtaposes Cys residues in exposed loops that form disulfide bonds within the oxidative environment of the IMS (**Fig. 2B, 2D, fig. S7B, supplementary text**). On the cytosolic side, a pi-pi interaction between symmetric Pro116 residues on the β6–β7 loops is further braced by PINK1 Arg426 (**Fig. 2C).** A previous crystal structure of a zebrafish VDAC2 dimer (**Fig. 2D**)(*45*) formed symmetrically through β-strands 17-19, 1 and 3. In our structure, this hydrophobic VDAC2 surface is occupied by TOM5 on both molecules and is further strengthened by a salt bridge (TOM5-Lys47:VDAC2-Asp239) (**Fig. 2E, fig S8**). VDAC2 Asp239 and the hydrophobic residues are largely conserved across all three VDAC isoforms (**fig. S9**).

TOM20 is a dynamically associated accessory subunit of the TOM complex that serves as a presequence receptor (*29*). How TOM20 engages with the TOM core complex upon presequence recognition, and then interacts with TOM22 to enable presequence entry into the TOM40 barrel remains unclear. Previous studies used cross-linking to stabilize and visualize TOM20, achieving low local resolution reconstruction for these components (*38*, *39*). Our structure has enabled high-resolution reconstruction of TOM20 and TOM22 in an arrested state of the TOM complex with a stalled substrate.

Consistent with some previous reports (*39*, *46*), but contrary to others (*38*), only one TOM20 molecule per TOM core complex was observed. In our structure, TOM20 is resolved from residue 15-131 (**Fig. 2F**) and residues 15-24 are inserted into the membrane, between VDAC2 and TOM22, some 50 Å away from previously reported locations (*39*) (**fig S10A**). The cytoplasmic portion of TOM20 begins at Asp25, as a helical extension of the TM domain. This helix then kinks at Pro32 and continues to Ala52, culminating in the helical presequence binding domain that binds PINK1 (see below) (**Fig. 2F**). The kinked arrangement of TOM20 is cantilevered by the α3 and α4 helices of TOM22, likely through multiple aromatic and Van der Waals interactions, which, however, could not be confidently modelled in the final reconstruction (**Fig. 2G**). We were unable to model the α1 and α2 helices of TOM22, but we instead show that a previously published assignment of the TOM22 α1 and α2 helices (*38*) in fact coincides with our density for the transmembrane domain of TOM20 (**fig. S10B**). Using 3D variability analysis (3DVA), we resolved multiple conformations of the entire TOM20 N-terminus (**fig. S11**). In one 3DVA cluster, TOM20 extends towards the IMS side of the micelle and contacts the VDAC barrel (**fig. S11**). These analyses highlight the mobility of the TOM20 transmembrane region, explaining the difficulty in capturing this mobile TOM component (*38*, *39*). Hence, the arrested substrate PINK1 locks TOM20 (and TOM22) in a most peripheral location on the TOM complex close to VDAC2; in active, translocating TOM complexes, TOM20-TOM22 locations may be distinct.

Structure of human PINK1

We resolve in our structure, residues 63-581 of human PINK1, whereby residues 70-110 are located within the TOM40 barrel (**Fig 3A**). The cytosolic portion of PINK1, from residue 110 to C-terminus, folds into the anticipated extended kinase domain, similar to insect PINK1 orthologs

(*20*, *21*) (**Fig. 3B**). Moreover, PINK1 kinase domains form a symmetric dimer, stabilized by an inter-molecular disulfide at Cys166, at the tip of the kinase P-loop, also similar to *Ph*PINK1 Cys169-linked dimers (*21*) (**Fig. 3A, B**). Dimerization is essential for PINK1 to trans-autophosphorylate (on Ser202 in *Ph*PINK1, or Ser228 in human PINK1), which in *Ph*PINK1 induces conformational changes in the N-lobe, including αC helix kinking and ordering of insertion-3 to form the ubiquitin binding site (*21*, *47*). However, for *Ph*PINK1 to phosphorylate ubiquitin, the dimer must disassociate (*21*).

In our structure, human PINK1 adopts an active kinase conformation, with aligned C- and R-spines, and displays a kinked αC helix (*48*) suggesting that trans-autophosphorylation has taken place (**Fig. 3C, D**). However, density around Ser228 was too weak to model confidently, and was therefore modelled in the unphosphorylated state. Folding of insertion-3 is induced by phosphorylation (*21*, *47*), yet in our structure, insertion 3 remains disordered. Indeed, all three kinase domain insertions in human PINK1 (*19*) are disordered and were not modelled (**Fig. 3C**).

Closer examination of the dataset revealed substantial mobility in the kinase domains in particular. In fact, the high-resolution reconstruction was obtained from ~1/3 of all particles, reflecting those with Cys166 crosslinks, according to 3D classification without alignment. In the remaining ~2/3 of particles, dimers still formed with locked-in-place C-lobes, but disordered kinase N-lobes. In these particles, PINK1 molecules are likely not disulfide-linked, and able to dissociate, which is a prerequisite for ubiquitin phosphorylation. Alternatively, this large set of particles could simply represent air-water interface-damaged particles.

Together, the overall structure of human PINK1 kinase domain is highly consistent with structures and biochemistry performed for *Ph*PINK1 and *Tc*PINK1 (*20*, *21*, *47*, *49*), and confirms many aspects of the PINK1 activation cascade. We interpret our structure as a post-phosphorylation/ activation (kinked αC helix), yet pre-active (crosslinked dimer) state of the ubiquitin kinase PINK1.

Interactions of the human PINK1 dimer with the TOM-VDAC array

Two additional intramolecular disulfides further stabilize PINK1 on the TOM-VDAC array: between Cys125, a residue mutated in EOPD on the kinase domain N-helix, and Cys564 on the C-terminal αM helix, as well as between Cys549 on the αL helix, and Cys377 in the β7-β8 loop. Both disulfides lock the kinase N-helix (aa 106-134) to the C-lobe and intrinsically reinforce the kinase domain (**Fig. 3A, 3E**). The kinase dimer position on the TOM-VDAC array is further locked-down by interactions with TOM20 and TOM5, holding it firmly in position.

TOM20 directly binds the PINK1 C-lobe αK helix (aa 524-543) in the hydrophobic presequence binding groove, and forms additional hydrogen bonds with the PINK1 N-helix (**Fig. 3E, fig S12**). These interactions have recently been suggested by AlphaFold modelling (*35*, *37*) . Overall, TOM20 provides an elaborate brace around the locked-down PINK1 dimer (**Fig. 1E**).

A surprising and prominent second interaction exists between the cytosolic N-terminal portion of TOM5 and the C-lobe of PINK1. TOM5 residues 1-15 are intimately connected with a previously unappreciated C-lobe groove formed by the αM helix of PINK1 and the C-lobe core. Hence, TOM5 not only provides crucial TOM-VDAC interactions but also appears to play a role in orienting and supporting the kinase domain above the TOM-VDAC array (**Fig. 3F**). Together, TOM20 and TOM5, along with the cross-linked αM/L/K and N-helices, appear to be responsible

for restricting the orientation and flexibility of PINK1 on the surface of mitochondria, promoting dimerization and activation (*21*).

PINK1 passage through TOM40

The locked-down conformation of the PINK1 dimer spans a distance of ~85 Å between residues that enter TOM40, which does not fit within a single TOM core complex (< 80Å distance between TOM40 barrels), explaining the observation of a TOM-VDAC array (**Fig. 3A**). As a result, only one of the TOM40 barrels is occupied in each TOM core complex.

Our structure resolves a physiological substrate, PINK1, within the TOM40 barrel at 2.75-Å resolution, illuminating the path of a presequence substrate in a human TOM40 barrel (**Fig. 4A, B**). Crosslinking in yeast had mapped multiple routes for substrates to traverse the Tom40 barrel, following non-overlapping pathways along the inner lining of the barrel (*50–54*). In our structure, the kinase N-helix (aa 107-135) enters the TOM40 barrel at Arg119. Within TOM40, the PINK1 transmembrane domain (aa 76-105) forms a long loop (aa 96-105) that skirts the TOM40 barrel, before traversing the channel via a short helix (aa 76-91). Four residues (aa 92-96) that include Cys92 and Cys96, are mobile and were not modelled. Cys92 is interesting as its role as a patient mutation has remained obscure (*32*, *55*, *56*).

PINK1 interacts via five surface segments with TOM40, namely *entrance*, *patch-1*, *patch-2*, *N-terminal segment* and *exit* (**Fig. 4A**). The cytosolic *entrance* for PINK1 is located on the cytosolic rim of TOM40, along β9 to β11. The PINK1 N-helix makes further interactions with the TOM7 N-terminus (Lys7) and more intriguingly, also with a phospholipid, PL4 (**fig. S5**), which forms hydrogen bonds via its phosphate head group with both PINK1 Arg119 and TOM7 Gln20 (**Fig. 4C, D**). Phospholipids at the TOM complex have previously been reported to be required for TOM complex stability and for binding of precursor substrates to the TOM complex (*57*), but a direct interaction between a substrate and phospholipid at the TOM complex has not been noted. Three additional charged interactions (PINK1 Arg119, Lys114, Glu114 with TOM20 Asp209, Glu243, Arg293) and hydrophobic contacts via PINK1 Leu108 and Leu110 stabilize PINK1 entry into the TOM40 barrel (**Fig. 4A-D**).

Patch-1 in the TOM40 barrel forms a channel along the curvature of the barrel, parallel to the membrane. Although it presents a net-negatively charged surface, *patch-1* binds a mostly hydrophobic PINK1 motif (sequence GRAVFLAFG, residues 97-105, **Fig. 4B**). In particular, TOM40 Glu234, located within an acidic patch just below the entrance forms hydrogen bonds with the backbone amides of Phe104 and Gly105. *Patch-2* forms a path down the channel and is also lined with acidic residues. This site is occupied by a short PINK1 helix (aa 76-91), which follows along β-strands 4 and 5 towards the IMS before protruding into the barrel β3-β4 loop of TOM40, stabilized by TOM40 Glu145. The TOM40 *N-terminal segment*, a short helix within the pore (**Fig. 4A***, right*), harnesses PINK1 as it traverses *patch-1* and *patch-2*, forming multiple interactions along its length. Here, TOM40 Phe83, situated within a pocket in *patch-1*, forms a pi-pi stack with PINK1 Phe104, and TOM40 Glu92 forms hydrogen bonds with PINK1 Arg80.

PINK1 *exits* TOM40 between strands β1 and β19, interacting with the TOM40 C-terminus at Gly361 (**Fig. 4A, B**). On the IMS rim of the TOM40 barrel, PINK1 forms hydrophobic and cation-pi interactions between PINK1 Phe69 and TOM40 Val105 and Lys107, and a β-sheet-like H-bonding network between the β1 strand of TOM40 and the PINK1 backbone between Arg68

and Phe70 (**Fig. 4E**). Further detailed analysis of changes within the TOM40 barrel, with and without a substrate, can be found in **Supplementary Text** and **fig. S13**.

We resolve six PINK1 residues (aa 63-69) emerging from TOM40, and interestingly, these are guided out of the barrel by TOM22 and TOM7. TOM22 interacts with PINK1 through a salt bridge between TOM22 Glu104, and invariant PINK1 Arg66, and through a hydrophobic contact (TOM22 Met108: PINK1 Leu63) (**Fig. 4E**). Similarly, the saxophone shape of TOM7 at the IMS side creates a pocket for Arg68 of PINK1 which forms three hydrogen bonds: with the backbone carbonyls of TOM7 Pro45 and TOM40 Leu109, and with the side chain of TOM7 Ser51. The 'elbow' of TOM7 is further stabilized by Van der Waals interactions between PINK1 Leu67 and TOM7 Pro45 (**Fig. 4E**). Importantly, both TOM7 interacting residues, PINK1 Arg68 and Leu67, are mutated in EOPD patients. TOM7 is known to be an important component of PINK1 stabilization (*35*, *58*). Deletion of TOM7 in human cells leads to continuous PINK1 import and cleavage (by OMA1) in depolarized conditions (*33*), and our structure explains how TOM7 guides the entrance and exit of PINK1 through the TOM complex and into mitochondria.

Conclusion - model for PINK1 stabilization on the TOM-VDAC array

Our structure of human PINK1 trapped as an import intermediate, apart from providing a structural explanation for PINK1 stabilization at the TOM complex and patient mutations in EOPD (**fig. S14**), answers the long-standing question of how a physiological presequence import substrate traffics through the human TOM complex. Unexpectedly, we also elucidated the architecture of a human VDAC2 dimer, which is the central component of the observed TOM-VDAC array, revealing a previously unknown role for the long-standing small TOM subunits, TOM5 (*59*). The yeast homolog of VDAC, porin, has been shown to be linked to protein import through its role in the mitochondrial carrier pathway and the Mitochondrial Intermembrane space Assembly (MIA) pathway (*60*, *61*). Yeast porin has the ability to regulate oligomerization of yeast Tom40 by sequestering Tom22 and a complexome profiling study observed TOM-porin and TOM-VDAC complexes in yeast and human mitochondria respectively (*60–62*). Our study now implicates TOM-VDAC association in the context of PINK1 mitophagy. It is unclear how common a feature the TOM-VDAC array is for the outer membrane landscape and whether it has roles in mitochondrial protein import in mammalian cells.

VDACs are the most abundant components of the MOM overall, and also the earliest and most abundantly ubiquitinated proteins on the MOM (*18*). Mapping of reported ubiquitination sites onto VDAC2 (*18*) in the complex structure (**fig. S15**), reveals that ubiquitination would disrupt the complex. However, a ubiquitinated VDAC may become a prime substrate for TOM-associated monomeric, PINK1 (**Fig. 5**). The role of VDAC in PINK1-mediated mitophagy has been debated, although the discussion has largely centered on VDAC1 (*63*, *64*). It has since been shown that depletion of all VDAC isoforms compromises Parkin recruitment to mitochondria (*65*) and that VDAC isoforms can even form a complex with Parkin (*66*). However, it was not expected that VDAC is a part of the PINK1 stabilization complex (*32*, *35*, *67*) and it remains to be determined whether VDAC2 has a role for PINK1 stabilization or activity.

To arrive at the stage of PINK1 entrapment visualized in our reconstruction, numerous preceding import steps would have taken place (**Fig. 5**). The PINK1 N-terminal presequence would be recognized by TOM complex receptors including TOM20 and TOM22, which would facilitate the import of the PINK1 N-terminus through the TOM40 barrel, exiting at an exit tunnel comprising TOM40, TOM7 and TOM22 (**Fig. 4E**). A similar exit for presequence substrates has been suggested in yeast (**fig. S13E**) (*50*, *54*, *68–70*). The presequence would be picked up by

TIM23 complex components TIM50 and TIM17B, which co-purify and form crosslinks with PINK1 (**Fig. 1C, fig. S3**), and which lead to cleavage and degradation of PINK1 in healthy mitochondria (**Fig. 5**). Depolarization would have inactivated the driving force for TIM23 translocation, blocking PINK1 import through the inner membrane and resulting in the accumulation of folded PINK1 bound to the TOM complex.

For PINK1 to become a ubiquitin kinase and signal mitochondrial dysfunction, it needs to dimerize and trans-autophosphorylate (*20*, *21*). PINK1 dimerization cannot occur within the same TOM core complex, but requires two TOM core complexes to assemble on a central VDAC dimer (**Fig. 5**). TOM5 plays integral roles to connect the TOM40 and VDAC β-barrels, and further provides a cytosolic docking site for PINK1. Also, TOM20, at the periphery of the TOM core complex in our structure, and in close proximity to VDAC2, provides an elaborate brace for the PINK1 dimer, which as a result is highly constrained on the MOM surface. Oxidation and disulfide bond-formation clearly contributed to the high-resolution structure presented here (**Fig. 5**). These oxidation events were not engineered (no cross-linkers or exogenous ROS for structural studies, SEC in presence of reducing agents) and likely reflect modification by endogenous ROS after depolarization. It is tempting to speculate that PINK1 oxidation is enhanced by VDAC channels exuding ROS during depolarization.

Dimerization prevents PINK1 from acting as a ubiquitin kinase (*21*), and to signal mitochondrial stress, the PINK1 dimer has to open, which for our structure would require reductive resolution of the Cys166 disulfide bridge. The resulting TOM-bound monomeric, active PINK1 may destabilize the TOM-VDAC array. At this point, ubiquitinated VDAC molecules would be presented with two docking sites: while TOM5 can bind the VDAC barrel, TOM associated PINK1 would bind and phosphorylate ubiquitin attached to VDAC. This model is consistent with earlier observations of VDAC-dependent Parkin recruitment (*65*, *66*). Parkin recruitment to phospho-ubiquitinated VDAC, would locate Parkin in close proximity to PINK1, streamlining Parkin activation by PINK1 (**Fig. 5**).

Next, we shall attempt to visualize PINK1 as an active ubiquitin kinase on mitochondria, as well as complete our structural studies of the PINK1-TOM-TIM23 supercomplex, which appeared to be present in a small number of particles but requires further stabilization. Our structure also provides multiple unexplored avenues to stabilize PINK1 on mitochondria, to develop much needed treatment options for Parkinson's disease patients.

References and Notes

Acknowledgments: We thank Michael Lazarou, Grant Dewson, Thanh Nguyen, Winnie Tan (WEHI), for helpful advice. We acknowledge use of the facilities at the Ian Holmes Imaging Centre, Bio21 Institute.

Funding:
National Health and Medical Research Council Investigator grant GNT1178122 (DK)
Australian Government Research Training Program Fellowship (ZYG)
The Hugo Christopher Middendorp Testamentary Trust (SC)
CSL Centenary Fellowship (AG)

Author contributions:

Conceptualization: SC, DK

Methodology: SC, NK, ZYG, TD, SAC, AL, LFD, AG

Cryo EM data collection: NK, AL

Structural modelling and refinement: NK, AG

Investigation: SC, NK, ZYG, TD, SAC, AL, LFD, AG

Visualization: SC, NK

Funding acquisition: SC, DK, AG

Supervision: SC, DK, AG

Writing – original draft: SC, NK, DK

Writing – review & editing: all authors.

Competing interests: DK is founder, shareholder and scientific advisory board member of Entact Bio and Proxima Bio. All other authors declare no competing interests.

Data and materials availability: Structural data and electron density maps for the entire complex, the symmetry expanded portion of the complex and the symmetry expanded with extended TOM20 helix have been submitted to the Protein Data Bank, with accession numbers 9EIH, 9EII and 9EIJ respectively, and EMDB accession numbers EMD-48083, EMD-48084, EMD-48085. The mass spectrometry proteomics data related to in-gel digests have been deposited to the ProteomeXchange Consortium via the PRIDE partner repository [dataset identifier PXD058526] (*71*). The SDA crosslinking mass spectrometry data have been deposited to the ProteomeXchange Consortium (*72*) via jPOST with accession number JPST003503.

Supplementary Materials

Materials and Methods

Supplementary Text

Figs. S1 to S15

Tables S1 to S2

Data S1 to S2

References 73-88

Fig. 1. Cryo-EM analysis of purified human PINK1-translocase complexes from mitochondria resolves dimerized PINK1 bound to a TOM-VDAC array. (A) Size exclusion chromatography (SEC) profile of purified PINK1-TOM-TIM23 complex. **(B)** The isolated PINK1-3×FLAG complex was run on a NuPAGE 4-12% Bis-Tris gel, western blotted and probed using the indicated antibodies. $N = 2$ independent experiments. **(C)** After SEC, fractions of PINK1-3×FLAG complexes containing both TOM and TIM23 components were pooled and loaded on a NuPAGE 4-12% Bis-Tris gel and stained using Instant Blue SafeStain (Expedeon). Prominent bands were excised, trypsin digested and identified using LC-MS. See **Data S1**. **(D)** A 3.1Å-resolution cryo-EM reconstruction of dimerized PINK1 bound to a TOM-VDAC array within a micelle is shown along the membrane plane and **(E)** from the cytosol and from the IMS. A composite density map is depicted, assembled from the density map of the overall refined complex (with all components colored) and overlaid with the outline of the unsharpened cryo-EM map of the micelle. The cryo-EM map of the micelle was generated using Chimera X by segmenting the unsharpened density map to remove PINK1, thereby isolating the micellar region surrounding the TOM-VDAC array. **(F)** The atomic model of the PINK-TOM-VDAC array, viewed along the membrane plane.

Fig. 2. PINK1 co-isolates with a unique TOM-VDAC2 assembly. (A) Atomic model of the TOM-VDAC array as viewed from the IMS. PINK1 has been removed from the model to emphasize the composition of the TOM-VDAC assembly. Phospholipids (PL) are numbered (see **fig. S5**). **(B)** Model of the isolated VDAC2 dimers viewed along membrane plane and overlayed on the cryoEM density. Disulfide bonds are shown as yellow spheres. Also see **fig. S6**. **(C)** Inset from (B) showing a close-up of the VDAC2 β6-β7 loop and its interaction with PINK1. Interacting residues are shown. **(D)** Model of VDAC2 homodimer from this structure overlayed on the model of the previously published zebrafish VDAC2 dimer (*45*). View is from the IMS and disulfide bonds are shown as yellow spheres. **(E)** Atomic model of TOM5 connecting the TOM40 barrel to VDAC2 viewed along the membrane plane. Inset shows a close-up of the TOM5-VDAC2 interaction interface. The sidechains of interacting residues are shown and hydrogen bonds are denoted by dotted blue lines. **(F)** Model of TOM20 along the membrane plane overlayed on the density for TOM20. PINK1 is removed from the model to more clearly depict TOM20. **(G)** Closeup of the interaction between TOM20 and TOM22 in the cytosolic space, overlayed on the cryoEM density (in mesh). The TOM22 α3 helix could not be confidently modelled and so only the density is shown. Sideview in Chimera X was used to enhance visualization of the interacting helices.

Fig. 3. Disulfide bonds stabilize a post activation, but pre-active PINK1 dimer. (A) Atomic model of PINK1 dimer overlayed on an outline of the density of the TOM-VDAC array. Disulfide bonds are depicted as yellow spheres. Dashed lines indicate unmodelled residues. Inset depicts the cryoEM density (mesh) for the disulfide bond between PINK1 C166. **(B)** Surface rendered models of the PINK1 dimer from this structure of *Hs*PINK1 and previously published *Ph*PINK1(*21*), as viewed from the top. TOM20 in the *Hs*PINK1 model is shown in ribbon form. **(C)** Typical active kinase features of *Hs*PINK1, depicted as atoms are the HRD (yellow) and DGF (blue) motifs, the αC-helix (orange) in the kinked conformation, hinge region (green), with catalytic spine (grey surface) and regulatory spine (white surface) in the aligned active conformation. Disordered loops are depicted as dotted lines. **(D)** Close up of the kinked αC helix for *Hs*PINK1 in our structure, alongside the straight αC helix in the published unphosphorylated *Ph*PINK1 (7T3X) and the kinked αC helix in phosphorylated *Ph*PINK1 (7T4K). **(E)** Close up of PINK1 bound to TOM20. For TOM20, the atomic model is shown within the surface model, colored to depict hydrophobicity. Disulfide bonds are shown as yellow spheres. **(F)** Close up of the interaction between the kinase lobe of PINK1 and the N-terminus of TOM5. Only sidechains for interacting residues that could be confidently modelled are shown. Disulfide bonds are depicted as yellow spheres.

Fig. 4. PINK1 illuminates a path for mitochondrial presequence substrates through the TOM40 barrel. (A) Atomic model of the asymmetric TOM40 barrel containing PINK1, along the membrane plane and viewed from the cytosol. Sidechains for residues that interact with PINK1 are shown. For visualization inside the barrel, β-strands 15-19 which are not contacted by PINK1, were removed. The indicated patches mark the different interaction regions of PINK1 through the barrel. **(B)** Surface electrostatic potential of the asymmetric TOM40 barrel, along the membrane plane, containing PINK1. A ribbon model is used to depict PINK1. Interacting side chains are shown. Sideview in Chimera X was used to segment the TOM40 barrel to enable visualization inside. **(C)** Interactions of PINK1 upon entrance and exit of the TOM40 barrel. TOM40 is shown as a surface rendered model, while PINK1 and TOM7 are in ribbon form. **(D)** A close-up of the PINK1 entrance into the TOM40 barrel from (C). PL indicates the phospholipid, shown in stick form. **(E)** A close-up of the PINK1 exit tunnel through the TOM40 barrel from (C). Interacting sidechains are shown.

Fig. 5. Model for PINK1 stabilization and proposed role of VDAC in the initiation of PINK1/Parkin mitophagy. Model of PINK1 stabilization and activity. 1. In healthy mitochondria, PINK1 is imported into the inner mitochondrial membrane in a membrane potential dependent ($\Delta\Psi$) manner via the TOM-TIM23 presequence pathway, before cleavage by PARL and retrotranslocation. 2. In depolarized mitochondria, PINK1 import into the inner membrane is blocked. The PINK1 kinase domain folds on the outer membrane. Simultaneously, ROS also stimulate VDAC2 dimerization in the IMS, as well as the dimerization of PINK1 molecules on separate TOM complexes. The PINK1-TOM-VDAC array thus assembles and PINK1 is trans-autophosphorylated. 3. As the initial burst of ROS dissipates and the redox environment becomes more reductive, the array and the PINK1 dimers dissociate. The associated VDACs can then either become ubiquitinated by a nearby E3 ligase, or since folded activated PINK1 can bind ubiquitin, the in-situ VDAC could be exchanged for an already ubiquitinated VDAC via avidity effects. 4. Ubiquitinated VDAC then becomes the prime PINK1 substrate and the resulting phosphoubiquitin recruits Parkin in close proximity to PINK1 to enable Parkin phosphorylation.

References

1. E. M. Valente, P. M. Abou-Sleiman, V. Caputo, M. M. K. Muqit, K. Harvey, S. Gispert, Z. Ali, D. D. Turco, A. R. Bentivoglio, D. G. Healy, A. Albanese, R. Nussbaum, R. González-Maldonado, T. Deller, S. Salvi, P. Cortelli, W. P. Gilks, D. S. Latchman, R. J. Harvey, B. Dallapiccola, G. Auburger, N. W. Wood, Hereditary early-onset Parkinson's disease caused by mutations in PINK1. *Science (New York, NY)* **304**, 1158–1160 (2004).

2. L. A. Kane, M. Lazarou, A. I. Fogel, Y. Li, K. Yamano, S. A. Sarraf, S. Banerjee, R. J. Youle, PINK1 phosphorylates ubiquitin to activate Parkin E3 ubiquitin ligase activity. *J. Cell Biol.* **205**, 143–153 (2014).

3. C. Kondapalli, A. Kazlauskaite, N. Zhang, H. I. Woodroof, D. G. Campbell, R. Gourlay, L. Burchell, H. Walden, T. J. Macartney, M. Deak, A. Knebel, D. R. Alessi, M. M. K. Muqit, PINK1 is activated by mitochondrial membrane potential depolarization and stimulates Parkin E3 ligase activity by phosphorylating Serine 65. *Open Biology* **2**, 120080 (2012).

4. A. Kazlauskaite, C. Kondapalli, R. Gourlay, D. G. Campbell, M. S. Ritorto, K. Hofmann, D. R. Alessi, A. Knebel, M. Trost, M. M. K. Muqit, Parkin is activated by PINK1-dependent phosphorylation of ubiquitin at Ser65. *The Biochemical journal* **460**, 127–139 (2014).

5. F. Koyano, K. Okatsu, H. Kosako, Y. Tamura, E. Go, M. Kimura, Y. Kimura, H. Tsuchiya, H. Yoshihara, T. Hirokawa, T. Endo, E. A. Fon, J.-F. Trempe, Y. Saeki, K. Tanaka, N. Matsuda, Ubiquitin is phosphorylated by PINK1 to activate parkin. *Nature* **510**, 162–166 (2014).

6. T. Wauer, K. N. Swatek, J. L. Wagstaff, C. Gladkova, J. N. Pruneda, M. A. Michel, M. Gersch, C. M. Johnson, S. M. Freund, D. Komander, Ubiquitin Ser65 phosphorylation affects ubiquitin structure, chain assembly and hydrolysis. *EMBO J.* **34**, 307–325 (2015).

7. A. Ordureau, S. A. Sarraf, D. M. Duda, J.-M. Heo, M. P. Jedrychowski, V. O. Sviderskiy, J. L. Olszewski, J. T. Koerber, T. Xie, S. A. Beausoleil, J. A. Wells, S. P. Gygi, B. A. Schulman, J. W. Harper, Quantitative Proteomics Reveal a Feedforward Mechanism for Mitochondrial PARKIN Translocation and Ubiquitin Chain Synthesis. *Molecular Cell* **56**, 360–375 (2014).

8. J. W. Harper, A. Ordureau, J.-M. Heo, Building and decoding ubiquitin chains for mitophagy. *Nat. Rev. Mol. Cell Biol.* **19**, 93–108 (2018).

9. M. F. Schmidt, Z. Y. Gan, D. Komander, G. Dewson, Ubiquitin signalling in neurodegeneration: mechanisms and therapeutic opportunities. *Cell Death Differ* **28**, 570–590 (2021).

10. D. P. Narendra, R. J. Youle, The role of PINK1–Parkin in mitochondrial quality control. *Nat. Cell Biol.* **26**, 1639–1651 (2024).

11. S. A. Sarraf, M. Raman, V. Guarani-Pereira, M. E. Sowa, E. L. Huttlin, S. P. Gygi, J. W. Harper, Landscape of the PARKIN-dependent ubiquitylome in response to mitochondrial depolarization. *Nature* **496**, 372–376 (2013).

12. T. Wauer, M. Simicek, A. F. Schubert, D. Komander, Mechanism of phospho-ubiquitin-induced PARKIN activation. *Nature* **524**, 370–374 (2015).

13. C. Gladkova, S. L. Maslen, J. M. Skehel, D. Komander, Mechanism of parkin activation by PINK1. *Nature* **559**, 410–414 (2018).

14. V. Sauvé, G. Sung, N. Soya, G. Kozlov, N. Blaimschein, L. S. Miotto, J.-F. Trempe, G. L. Lukacs, K. Gehring, Mechanism of parkin activation by phosphorylation. *Nature Structural & Molecular Biology* **25**, 623–630 (2018).

15. K. N. Swatek, J. L. Usher, A. F. Kueck, C. Gladkova, T. E. T. Mevissen, J. N. Pruneda, T. Skern, D. Komander, Insights into ubiquitin chain architecture using Ub-clipping. *Nature* **572**, 533–537 (2019).

16. O. Antico, A. Ordureau, M. Stevens, F. Singh, R. S. Nirujogi, M. Gierlinski, E. Barini, M. L. Rickwood, A. Prescott, R. Toth, I. G. Ganley, J. W. Harper, M. M. K. Muqit, Global ubiquitylation analysis of mitochondria in primary neurons identifies endogenous Parkin targets following activation of PINK1. *Sci. Adv.* **7**, eabj0722 (2021).

17. A. Ordureau, J. A. Paulo, J. Zhang, H. An, K. N. Swatek, J. R. Cannon, Q. Wan, D. Komander, J. W. Harper, Global Landscape and Dynamics of Parkin and USP30-Dependent Ubiquitylomes in iNeurons during Mitophagic Signaling. *Mol Cell* **77**, 1124-1142.e10 (2020).

18. A. Ordureau, J. A. Paulo, W. Zhang, T. Ahfeldt, J. Zhang, E. F. Cohn, Z. Hou, J.-M. Heo, L. L. Rubin, S. S. Sidhu, S. P. Gygi, J. W. Harper, Dynamics of PARKIN-Dependent Mitochondrial Ubiquitylation in Induced Neurons and Model Systems Revealed by Digital Snapshot Proteomics. *Molecular Cell* **70**, 211-227.e8 (2018).

19. H. I. Woodroof, J. H. Pogson, M. Begley, L. C. Cantley, M. Deak, D. G. Campbell, D. M. F. van Aalten, A. J. Whitworth, D. R. Alessi, M. M. K. Muqit, Discovery of catalytically active orthologues of the Parkinson's disease kinase PINK1: analysis of substrate specificity and impact of mutations. *Open Biology* **1**, 110012 (2011).

20. S. Rasool, S. Veyron, N. Soya, M. A. Eldeeb, G. L. Lukacs, E. A. Fon, J.-F. Trempe, Mechanism of PINK1 activation by autophosphorylation and insights into assembly on the TOM complex. *Mol Cell* **82**, 44-59.e6 (2022).

21. Z. Y. Gan, S. Callegari, S. A. Cobbold, T. R. Cotton, M. J. Mlodzianoski, A. F. Schubert, N. D. Geoghegan, K. L. Rogers, A. Leis, G. Dewson, A. Glukhova, D. Komander, Activation mechanism of PINK1. *Nature* **602**, 328–335 (2022).

22. A. Kumar, J. Tamjar, A. D. Waddell, H. I. Woodroof, O. G. Raimi, A. M. Shaw, M. Peggie, M. M. Muqit, D. M. van Aalten, Structure of PINK1 and mechanisms of Parkinson's disease-associated mutations. *Elife* **6**, e29985 (2017).

23. A. M. Pickrell, R. J. Youle, The Roles of PINK1, Parkin, and Mitochondrial Fidelity in Parkinson's Disease. *Neuron* **85**, 257–273 (2015).

24. N. T. Hertz, A. Berthet, M. L. Sos, K. S. Thorn, A. L. Burlingame, K. Nakamura, K. M. Shokat, A neo-substrate that amplifies catalytic activity of parkinson's-disease-related kinase PINK1. *Cell* **154**, 737–747 (2013).

25. N. Hertz, R. Chin, R. Rakhit, D. Ditsworth, C. Wang, J. Bartholomeus, S. Liu, A. Mody, A. Laihsu, A. Eastes, C. Tai, R. Kim, J. Li, S. Khasnavis, V. Rafalski, D. Heerendeen, V. Garda, J. Phung, D. de Roulet, A. Ordureau, J. W. Harper, S. Johnstone, J. Stöhr, Pharmacological PINK1 activation ameliorates Pathology in Parkinson's Disease models. *Res. Sq.*, rs.3.rs-4356493 (2024).

26. Z. Y. Gan, S. Callegari, T. N. Nguyen, N. S. Kirk, A. Leis, M. Lazarou, G. Dewson, D. Komander, Interaction of PINK1 with nucleotides and kinetin. *Sci. Adv.* **10**, eadj7408 (2024).

27. N. Pfanner, B. Warscheid, N. Wiedemann, Mitochondrial proteins: from biogenesis to functional networks. *Nat. Rev. Mol. Cell Biol.* **20**, 267–284 (2019).

28. J. D. Busch, L. F. Fielden, N. Pfanner, N. Wiedemann, Mitochondrial protein transport: Versatility of translocases and mechanisms. *Mol. Cell* **83**, 890–910 (2023).

29. Y. Araiso, K. Imai, T. Endo, Role of the TOM Complex in Protein Import into Mitochondria: Structural Views. *Annu. Rev. Biochem.* **91**, 679–703 (2022).

30. S. Callegari, L. D. Cruz-Zaragoza, P. Rehling, From TOM to the TIM23 complex – handing over of a precursor. *Biol. Chem.* **401**, 709–721 (2020).

31. M. Lazarou, S. M. Jin, L. A. Kane, R. J. Youle, Role of PINK1 binding to the TOM complex and alternate intracellular membranes in recruitment and activation of the E3 ligase Parkin. *Developmental cell* **22**, 320–333 (2012).

32. K. Okatsu, M. Uno, F. Koyano, E. Go, M. Kimura, T. Oka, K. Tanaka, N. Matsuda, A dimeric PINK1-containing complex on depolarized mitochondria stimulates Parkin recruitment. *The Journal of biological chemistry* **288**, 36372–36384 (2013).

33. S. Sekine, C. Wang, D. P. Sideris, E. Bunker, Z. Zhang, R. J. Youle, Reciprocal Roles of Tom7 and OMA1 during Mitochondrial Import and Activation of PINK1. *Molecular Cell* **73**, 1028-1043.e5 (2019).

34. M. A. Eldeeb, A. N. Bayne, A. Fallahi, T. Goiran, E. J. MacDougall, A. Soumbasis, C. E. Zorca, J.-J. Tabah, R. A. Thomas, N. Karpilovsky, M. Mathur, T. M. Durcan, J.-F. Trempe, E. A.

Fon, Tom20 gates PINK1 activity and mediates its tethering of the TOM and TIM23 translocases upon mitochondrial stress. *Proc. Natl. Acad. Sci.* **121**, e2313540121 (2024).

35. O. G. Raimi, H. Ojha, K. Ehses, V. Dederer, S. M. Lange, C. P. Rivera, T. D. Deegan, Y. Chen, M. Wightman, R. Toth, K. P. M. Labib, S. Mathea, N. Ranson, R. Fernández-Busnadiego, M. M. K. Muqit, Mechanism of human PINK1 activation at the TOM complex in a reconstituted system. *Sci. Adv.* **10**, eadn7191 (2024).

36. S. Akabane, K. Watanabe, H. Kosako, S. Yamashita, K. Nishino, M. Kato, S. Sekine, T. Kanki, N. Matsuda, T. Endo, T. Oka, TIM23 facilitates PINK1 activation by safeguarding against OMA1-mediated degradation in damaged mitochondria. *Cell Rep.* **42**, 112454 (2023).

37. M. A. Eldeeb, A. N. Bayne, A. Fallahi, T. Goiran, E. J. MacDougall, A. Soumbasis, C. E. Zorca, J.-J. Tabah, R. A. Thomas, N. Karpilovsky, M. Mathur, T. M. Durcan, J.-F. Trempe, E. A. Fon, Tom20 gates PINK1 activity and mediates its tethering of the TOM and TIM23 translocases upon mitochondrial stress. *Proc. Natl. Acad. Sci.* **121**, e2313540121 (2024).

38. J. Su, D. Liu, F. Yang, M.-Q. Zuo, C. Li, M.-Q. Dong, S. Sun, S.-F. Sui, Structural basis of Tom20 and Tom22 cytosolic domains as the human TOM complex receptors. *Proc. Natl. Acad. Sci.* **119**, e2200158119 (2022).

39. J. Su, X. Tian, Z. Wang, J. Yang, S. Sun, S.-F. Sui, Structure of the intact Tom20 receptor in the human translocase of the outer membrane complex. *PNAS Nexus* **3**, pgae269 (2024).

40. W. Wang, X. Chen, L. Zhang, J. Yi, Q. Ma, J. Yin, W. Zhuo, J. Gu, M. Yang, Atomic structure of human TOM core complex. *Cell Discov* **6**, 67 (2020).

41. Z. Guan, L. Yan, Q. Wang, L. Qi, S. Hong, Z. Gong, C. Yan, P. Yin, Structural insights into assembly of human mitochondrial translocase TOM complex. *Cell Discov.* **7**, 22 (2021).

42. E. H.-Y. Cheng, T. V. Sheiko, J. K. Fisher, W. J. Craigen, S. J. Korsmeyer, VDAC2 Inhibits BAK Activation and Mitochondrial Apoptosis. *Science* **301**, 513–517 (2003).

43. H. L. Glover, A. Schreiner, G. Dewson, S. W. G. Tait, Mitochondria and cell death. *Nat. Cell Biol.* **26**, 1434–1446 (2024).

44. T. Hosaka, M. Okazaki, T. Kimura-Someya, Y. Ishizuka-Katsura, K. Ito, S. Yokoyama, K. Dodo, M. Sodeoka, M. Shirouzu, Crystal structural characterization reveals novel oligomeric interactions of human voltage-dependent anion channel 1. *Protein Sci.* **26**, 1749–1758 (2017).

45. J. Schredelseker, A. Paz, C. J. López, C. Altenbach, C. S. Leung, M. K. Drexler, J.-N. Chen, W. L. Hubbell, J. Abramson, High resolution structure and double electron-electron resonance of the zebrafish voltage-dependent anion channel 2 reveal an oligomeric population. *J. Biol. Chem.* **289**, 12566–77 (2014).

46. P. Ornelas, T. Bausewein, J. Martin, N. Morgner, S. Nussberger, W. Kühlbrandt, Two conformations of the Tom20 preprotein receptor in the TOM holo complex. *Proc. Natl. Acad. Sci.* **120**, e2301447120 (2023).

47. A. F. Schubert, C. Gladkova, E. Pardon, J. L. Wagstaff, S. M. V. Freund, J. Steyaert, S. L. Maslen, D. Komander, Structure of PINK1 in complex with its substrate ubiquitin. *Nature* **552**, 51–56 (2017).

48. S. S. Taylor, A. P. Kornev, Protein kinases: evolution of dynamic regulatory proteins. *Trends in Biochemical Sciences* **36**, 65–77 (2011).

49. K. Okatsu, Y. Sato, K. Yamano, N. Matsuda, L. Negishi, A. Takahashi, A. Yamagata, S. Goto-Ito, M. Mishima, Y. Ito, T. Oka, K. Tanaka, S. Fukai, Structural insights into ubiquitin phosphorylation by PINK1. *Sci. Rep.* **8**, 10382 (2018).

50. T. Shiota, K. Imai, J. Qiu, V. L. Hewitt, K. Tan, H.-H. Shen, N. Sakiyama, Y. Fukasawa, S. Hayat, M. Kamiya, A. Elofsson, K. Tomii, P. Horton, N. Wiedemann, N. Pfanner, T. Lithgow, T. Endo, Molecular architecture of the active mitochondrial protein gate. *Science* **349**, 1544–1548 (2015).

51. X. Zhou, Y. Yang, G. Wang, S. Wang, D. Sun, X. Ou, Y. Lian, L. Li, Molecular pathway of mitochondrial preprotein import through the TOM–TIM23 supercomplex. *Nat. Struct. Mol. Biol.* **30**, 1996–2008 (2023).

52. K. Tucker, E. Park, Cryo-EM structure of the mitochondrial protein-import channel TOM complex at near-atomic resolution. *Nat. Struct. Mol. Biol.* **26**, 1158–1166 (2019).

53. Y. Araiso, A. Tsutsumi, J. Suzuki, K. Yunoki, S. Kawano, M. Kikkawa, T. Endo, Cryo-EM structure of the translocator of the outer mitochondrial membrane. doi: 10.2210/pdb6jnf/pdb (2019).

54. T. Bausewein, D. J. Mills, J. D. Langer, B. Nitschke, S. Nussberger, W. Kühlbrandt, Cryo-EM Structure of the TOM Core Complex from Neurospora crassa. *Cell* **170**, 693-700.e7 (2017).

55. M. Iguchi, Y. Kujuro, K. Okatsu, F. Koyano, H. Kosako, M. Kimura, N. Suzuki, S. Uchiyama, K. Tanaka, N. Matsuda, Parkin-catalyzed Ubiquitin-Ester Transfer Is Triggered by PINK1-dependent Phosphorylation*. *J. Biol. Chem.* **288**, 22019–22032 (2013).

56. K. Okatsu, T. Oka, M. Iguchi, K. Imamura, H. Kosako, N. Tani, M. Kimura, E. Go, F. Koyano, M. Funayama, K. Shiba-Fukushima, S. Sato, H. Shimizu, Y. Fukunaga, H. Taniguchi, M. Komatsu, N. Hattori, K. Mihara, K. Tanaka, N. Matsuda, PINK1 autophosphorylation upon membrane potential dissipation is essential for Parkin recruitment to damaged mitochondria. *Nat. Commun.* **3**, 1016 (2012).

57. J. J. Hoffmann, T. Becker, Crosstalk between Mitochondrial Protein Import and Lipids. *Int. J. Mol. Sci.* **23**, 5274 (2022).

58. K. K. Maruszczak, M. Jung, S. Rasool, J.-F. Trempe, D. Rapaport, The role of the individual TOM subunits in the association of PINK1 with depolarized mitochondria. *J. Mol. Med.* **100**, 747–762 (2022).

59. K. Dietmeier, A. Hönlinger, U. Bömer, P. J. T. Dekker, C. Eckerskorn, F. Lottspeich, M. Kübrich, N. Pfanner, Tom5 functionally links mitochondrial preprotein receptors to the general import pore. *Nature* **388**, 195–200 (1997).

60. L. Ellenrieder, M. P. Dieterle, K. N. Doan, C. U. Mårtensson, A. Floerchinger, M. L. Campo, N. Pfanner, T. Becker, Dual Role of Mitochondrial Porin in Metabolite Transport across the Outer Membrane and Protein Transfer to the Inner Membrane. *Mol. Cell* **73**, 1056-1065.e7 (2019).

61. H. Sakaue, T. Shiota, N. Ishizaka, S. Kawano, Y. Tamura, K. S. Tan, K. Imai, C. Motono, T. Hirokawa, K. Taki, N. Miyata, O. Kuge, T. Lithgow, T. Endo, Porin Associates with Tom22 to Regulate the Mitochondrial Protein Gate Assembly. *Mol. Cell* **73**, 1044-1055.e8 (2019).

62. C. S. Müller, W. Bildl, A. Haupt, L. Ellenrieder, T. Becker, C. Hunte, B. Fakler, U. Schulte, Cryo-slicing Blue Native-Mass Spectrometry (csBN-MS), a Novel Technology for High Resolution Complexome Profiling*. *Mol. Cell. Proteom.* **15**, 669–681 (2016).

63. D. Narendra, L. A. Kane, D. N. Hauser, I. M. Fearnley, R. J. Youle, p62/SQSTM1 is required for Parkin-induced mitochondrial clustering but not mitophagy; VDAC1 is dispensable for both. *Autophagy* **6**, 1090–106 (2010).

64. S. Geisler, K. M. Holmström, D. Skujat, F. C. Fiesel, O. C. Rothfuss, P. J. Kahle, W. Springer, PINK1/Parkin-mediated mitophagy is dependent on VDAC1 and p62/SQSTM1. *Nat. Cell Biol.* **12**, 119–131 (2010).

65. Y. Sun, A. A. Vashisht, J. Tchieu, J. A. Wohlschlegel, L. Dreier, Voltage-dependent Anion Channels (VDACs) Recruit Parkin to Defective Mitochondria to Promote Mitochondrial Autophagy*. *J. Biol. Chem.* **287**, 40652–40660 (2012).

66. S. Callegari, S. Oeljeklaus, B. Warscheid, S. Dennerlein, M. Thumm, P. Rehling, J. Dudek, Phospho-ubiquitin-PARK2 complex as a marker for mitophagy defects. *Autophagy* **13**, 201–211 (2017).

67. M. Lazarou, S. M. Jin, L. A. Kane, R. J. Youle, Role of PINK1 binding to the TOM complex and alternate intracellular membranes in recruitment and activation of the E3 ligase Parkin. *Developmental cell* **22**, 320–333 (2012).

68. Y. Araiso, T. Endo, Structural overview of the translocase of the mitochondrial outer membrane complex. *Biophys. Physicobiology* **19**, n/a (2022).

69. X. Zhou, Y. Yang, G. Wang, S. Wang, D. Sun, X. Ou, Y. Lian, L. Li, Molecular pathway of mitochondrial preprotein import through the TOM–TIM23 supercomplex. *Nat. Struct. Mol. Biol.* **30**, 1996–2008 (2023).

70. K. Tucker, E. Park, Cryo-EM structure of the mitochondrial protein-import channel TOM complex at near-atomic resolution. *Nat. Struct. Mol. Biol.* **26**, 1158–1166 (2019).

71. Y. Perez-Riverol, J. Bai, C. Bandla, D. García-Seisdedos, S. Hewapathirana, S. Kamatchinathan, D. J. Kundu, A. Prakash, A. Frericks-Zipper, M. Eisenacher, M. Walzer, S. Wang, A. Brazma, J. A. Vizcaíno, The PRIDE database resources in 2022: a hub for mass spectrometry-based proteomics evidences. *Nucleic Acids Res.* **50**, D543–D552 (2021).

72. S. Okuda, Y. Watanabe, Y. Moriya, S. Kawano, T. Yamamoto, M. Matsumoto, T. Takami, D. Kobayashi, N. Araki, A. C. Yoshizawa, T. Tabata, N. Sugiyama, S. Goto, Y. Ishihama, jPOSTrepo: an international standard data repository for proteomes. *Nucleic Acids Res.* **45**, D1107–D1111 (2017).

73. G. O. Krasnoselska, M. Dumoux, N. Gamage, H. Cheruvara, J. Birch, A. Quigley, R. J. Owens, Transient Transfection and Expression of Eukaryotic Membrane Proteins in Expi293F Cells and Their Screening on a Small Scale: Application for Structural Studies. *Methods Mol. Biol. (Clifton, NJ)* **2305**, 105–128 (2021).

74. A. Valpadashi, S. Callegari, A. Linden, P. Neumann, R. Ficner, H. Urlaub, M. Deckers, P. Rehling, Defining the architecture of the human TIM22 complex by chemical crosslinking. *FEBS Lett.* **595**, 157–168 (2021).

75. R. Richter-Dennerlein, S. Oeljeklaus, I. Lorenzi, C. Ronsör, B. Bareth, A. B. Schendzielorz, C. Wang, B. Warscheid, P. Rehling, S. Dennerlein, Mitochondrial Protein Synthesis Adapts to Influx of Nuclear-Encoded Protein. *Cell* **167**, 471-483.e10 (2016).

76. J. Cox, N. Neuhauser, A. Michalski, R. A. Scheltema, J. V. Olsen, M. Mann, Andromeda: A Peptide Search Engine Integrated into the MaxQuant Environment. *J. Proteome Res.* **10**, 1794–1805 (2011).

77. M. C. Chambers, B. Maclean, R. Burke, D. Amodei, D. L. Ruderman, S. Neumann, L. Gatto, B. Fischer, B. Pratt, J. Egertson, K. Hoff, D. Kessner, N. Tasman, N. Shulman, B. Frewen, T. A. Baker, M.-Y. Brusniak, C. Paulse, D. Creasy, L. Flashner, K. Kani, C. Moulding, S. L. Seymour, L. M. Nuwaysir, B. Lefebvre, F. Kuhlmann, J. Roark, P. Rainer, S. Detlev, T. Hemenway, A. Huhmer, J. Langridge, B. Connolly, T. Chadick, K. Holly, J. Eckels, E. W. Deutsch, R. L. Moritz, J. E. Katz, D. B. Agus, M. MacCoss, D. L. Tabb, P. Mallick, A cross-platform toolkit for mass spectrometry and proteomics. *Nat. Biotechnol.* **30**, 918–920 (2012).

78. M. L. Mendes, L. Fischer, Z. A. Chen, M. Barbon, F. J. O'Reilly, S. H. Giese, M. Bohlke-Schneider, A. Belsom, T. Dau, C. W. Combe, M. Graham, M. R. Eisele, W. Baumeister, C. Speck, J. Rappsilber, An integrated workflow for crosslinking mass spectrometry. *Mol. Syst. Biol.* **15**, e8994 (2019).

79. C. W. Combe, M. Graham, L. Kolbowski, L. Fischer, J. Rappsilber, xiVIEW: Visualisation of Crosslinking Mass Spectrometry Data. *J. Mol. Biol.* **436**, 168656 (2024).

80. A. Punjani, J. L. Rubinstein, D. J. Fleet, M. A. Brubaker, cryoSPARC: algorithms for rapid unsupervised cryo-EM structure determination. *Nat. Methods* **14**, 290–296 (2017).

81. J. Abramson, J. Adler, J. Dunger, R. Evans, T. Green, A. Pritzel, O. Ronneberger, L. Willmore, A. J. Ballard, J. Bambrick, S. W. Bodenstein, D. A. Evans, C.-C. Hung, M. O'Neill, D. Reiman, K. Tunyasuvunakool, Z. Wu, A. Žemgulytė, E. Arvaniti, C. Beattie, O. Bertolli, A. Bridgland, A. Cherepanov, M. Congreve, A. I. Cowen-Rivers, A. Cowie, M. Figurnov, F. B. Fuchs, H. Gladman, R. Jain, Y. A. Khan, C. M. R. Low, K. Perlin, A. Potapenko, P. Savy, S. Singh, A. Stecula, A. Thillaisundaram, C. Tong, S. Yakneen, E. D. Zhong, M. Zielinski, A. Žídek, V. Bapst, P. Kohli, M. Jaderberg, D. Hassabis, J. M. Jumper, Accurate structure prediction of biomolecular interactions with AlphaFold 3. *Nature* **630**, 493–500 (2024).

82. E. C. Meng, T. D. Goddard, E. F. Pettersen, G. S. Couch, Z. J. Pearson, J. H. Morris, T. E. Ferrin, UCSF ChimeraX : Tools for structure building and analysis. *Protein Sci.* **32**, e4792 (2023).

83. T. I. Croll, ISOLDE: a physically realistic environment for model building into low-resolution electron-density maps. *Acta Crystallogr. Sect. D* **74**, 519–530 (2018).

84. P. Emsley, B. Lohkamp, W. G. Scott, K. Cowtan, Features and development of Coot. *Acta Crystallogr. Sect. D* **66**, 486–501 (2010).

85. D. Liebschner, P. V. Afonine, M. L. Baker, G. Bunkóczi, V. B. Chen, T. I. Croll, B. Hintze, L.-W. Hung, S. Jain, A. J. McCoy, N. W. Moriarty, R. D. Oeffner, B. K. Poon, M. G. Prisant, R. J. Read, J. S. Richardson, D. C. Richardson, M. D. Sammito, O. V. Sobolev, D. H. Stockwell, T. C. Terwilliger, A. G. Urzhumtsev, L. L. Videau, C. J. Williams, P. D. Adams, Macromolecular structure determination using X-rays, neutrons and electrons: recent developments in Phenix. *Acta Crystallogr. Sect. D, Struct. Biol.* **75**, 861–877 (2019).

86. V. D. Pinto, Renaissance of VDAC: New Insights on a Protein Family at the Interface between Mitochondria and Cytosol. *Biomolecules* **11**, 107 (2021).

87. G. G. Piroli, A. M. Manuel, A. C. Clapper, M. D. Walla, J. E. Baatz, R. D. Palmiter, A. Quintana, N. Frizzell, Succination is Increased on Select Proteins in the Brainstem of the NADH dehydrogenase (ubiquinone) Fe-S protein 4 (Ndufs4) Knockout Mouse, a Model of Leigh Syndrome*. *Mol. Cell. Proteom.* **15**, 445–461 (2016).

88. Q. Wang, J. Zhuang, R. Huang, Z. Guan, L. Yan, S. Hong, L. Zhang, C. Huang, Z. Liu, P. Yin, The architecture of substrate-engaged TOM–TIM23 supercomplex reveals preprotein proximity sites for mitochondrial protein translocation. *Cell Discov.* **10**, 19 (2024).

Figure 1

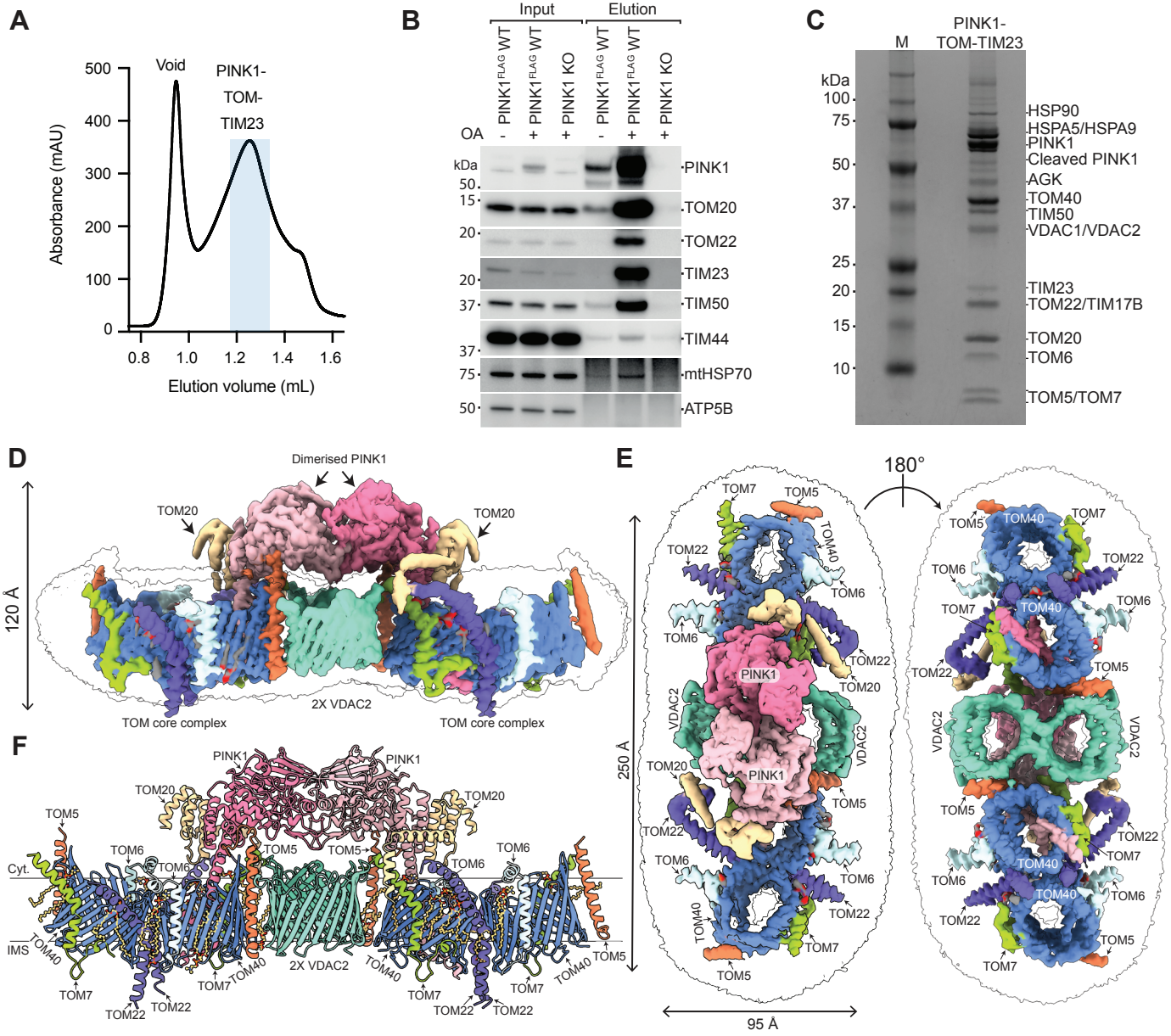
A
Void
PINK1-
TOM-
TIM23
Absorbance (mAU)
Elution volume (mL)
B
Input
Elution
PINK1FLAG WT
PINK1FLAG WT
PINK1 KO
PINK1FLAG WT
PINK1FLAG WT
PINK1 KO
OA
kDa
PINK1
TOM20
TOM22
TIM23
TIM50
TIM44
mtHSP70
ATP5B
C
M
PINK1-
TOM-TIM23
kDa
HSP90
HSPA5/HSPA9
PINK1
Cleaved PINK1
AGK
TOM40
TIM50
VDAC1/VDAC2
TIM23
TOM22/TIM17B
TOM20
TOM6
TOM5/TOM7
D
Dimerised PINK1
TOM20
TOM20
120 Å
TOM core complex
2X VDAC2
TOM core complex
E
180°
250 Å
95 Å
PINK1
VDAC2
F
PINK1
TOM20
TOM5
TOM6
Cyt.
IMS
TOM40
TOM7
TOM22
2X VDAC2

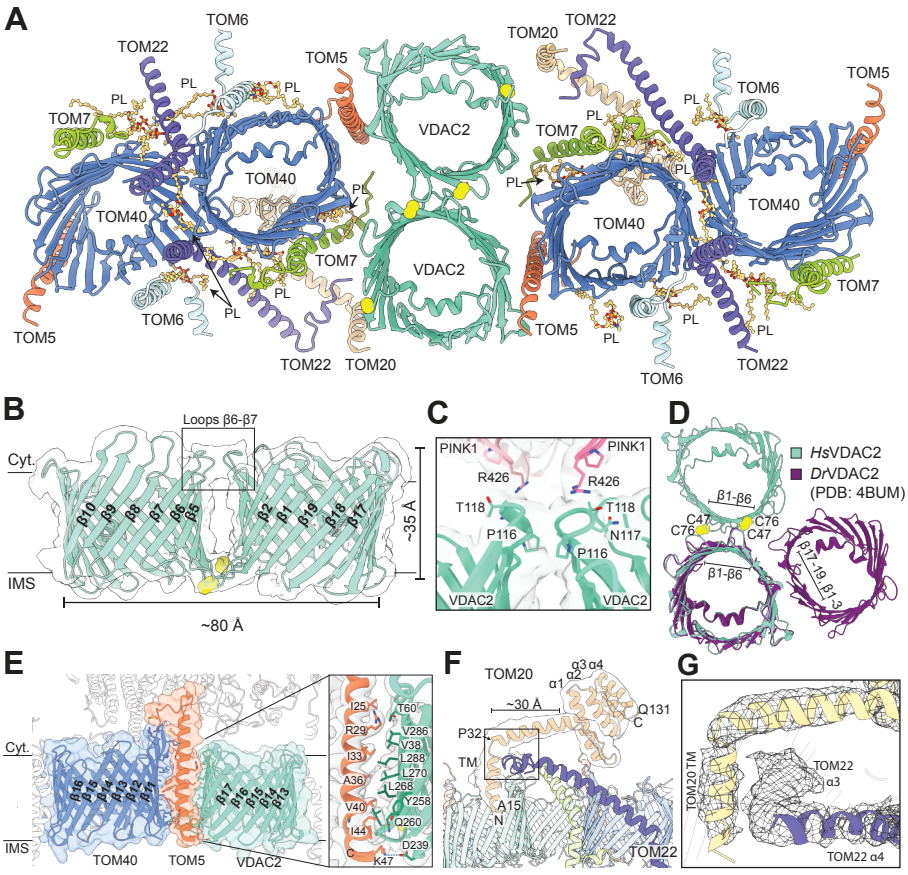
A
TOM6
TOM22
TOM5
TOM20
TOM7
PL
VDAC2
TOM40
TOM5
TOM6
TOM22
TOM20
B
Loops β6-β7
Cyt.
IMS
~35 Å
~80 Å
C
PINK1
R426
T118
P116
N117
VDAC2
D
HsVDAC2
DrVDAC2
(PDB: 4BUM)
β1-β6
C47
C76
E
Cyt.
IMS
TOM40
TOM5
VDAC2
F
TOM20
~30 Å
Q131
P32
TM
A15
TOM22
G
TOM20 TM
TOM22
α3
TOM22 α4

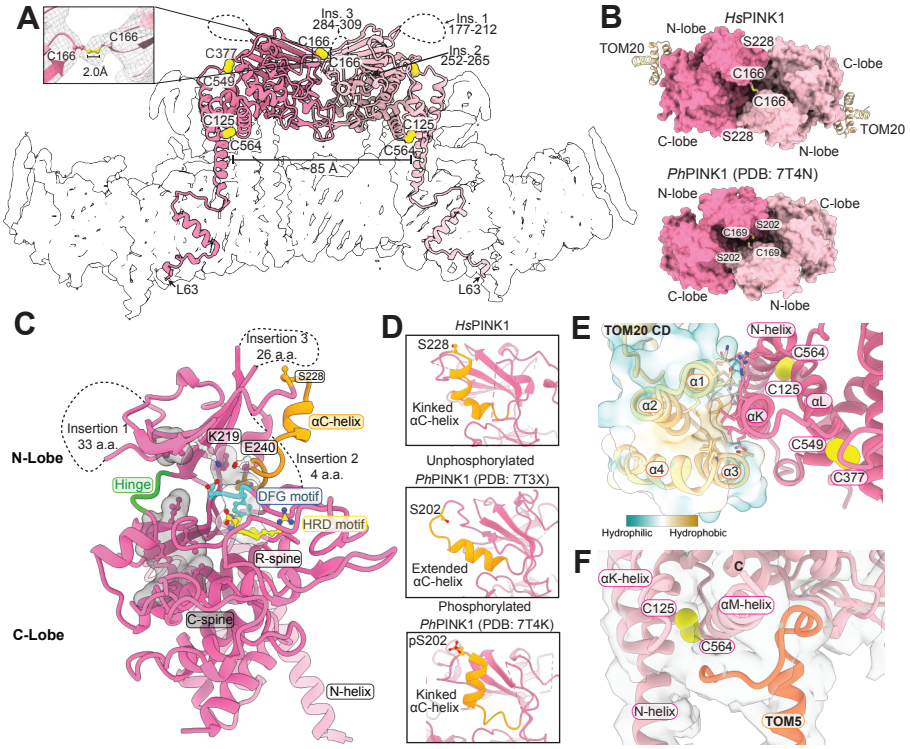
A
C166
C166
2.0Å
Ins. 3
284-309
Ins. 1
177-212
Ins. 2
252-265
C377
C166
C166
C549
C125
C125
C564
C564
85 Å
L63
L63
B
HsPINK1
N-lobe
S228
C-lobe
TOM20
C166
C166
C-lobe
S228
N-lobe
TOM20
PhPINK1 (PDB: 7T4N)
N-lobe
C-lobe
S202
C169
S202
C169
C-lobe
N-lobe
C
Insertion 3
26 a.a.
S228
αC-helix
Insertion 1
33 a.a.
K219
E240
Insertion 2
4 a.a.
N-Lobe
Hinge
DFG motif
HRD motif
R-spine
C-spine
C-Lobe
N-helix
D
HsPINK1
S228
Kinked
αC-helix
Unphosphorylated
PhPINK1 (PDB: 7T3X)
S202
Extended
αC-helix
Phosphorylated
PhPINK1 (PDB: 7T4K)
pS202
Kinked
αC-helix
E
TOM20 CD
N-helix
C564
α1
C125
αL
α2
αK
C549
α4
α3
C377
Hydrophilic
Hydrophobic
F
αK-helix
C
C125
αM-helix
C564
N-helix
TOM5

Figure 4

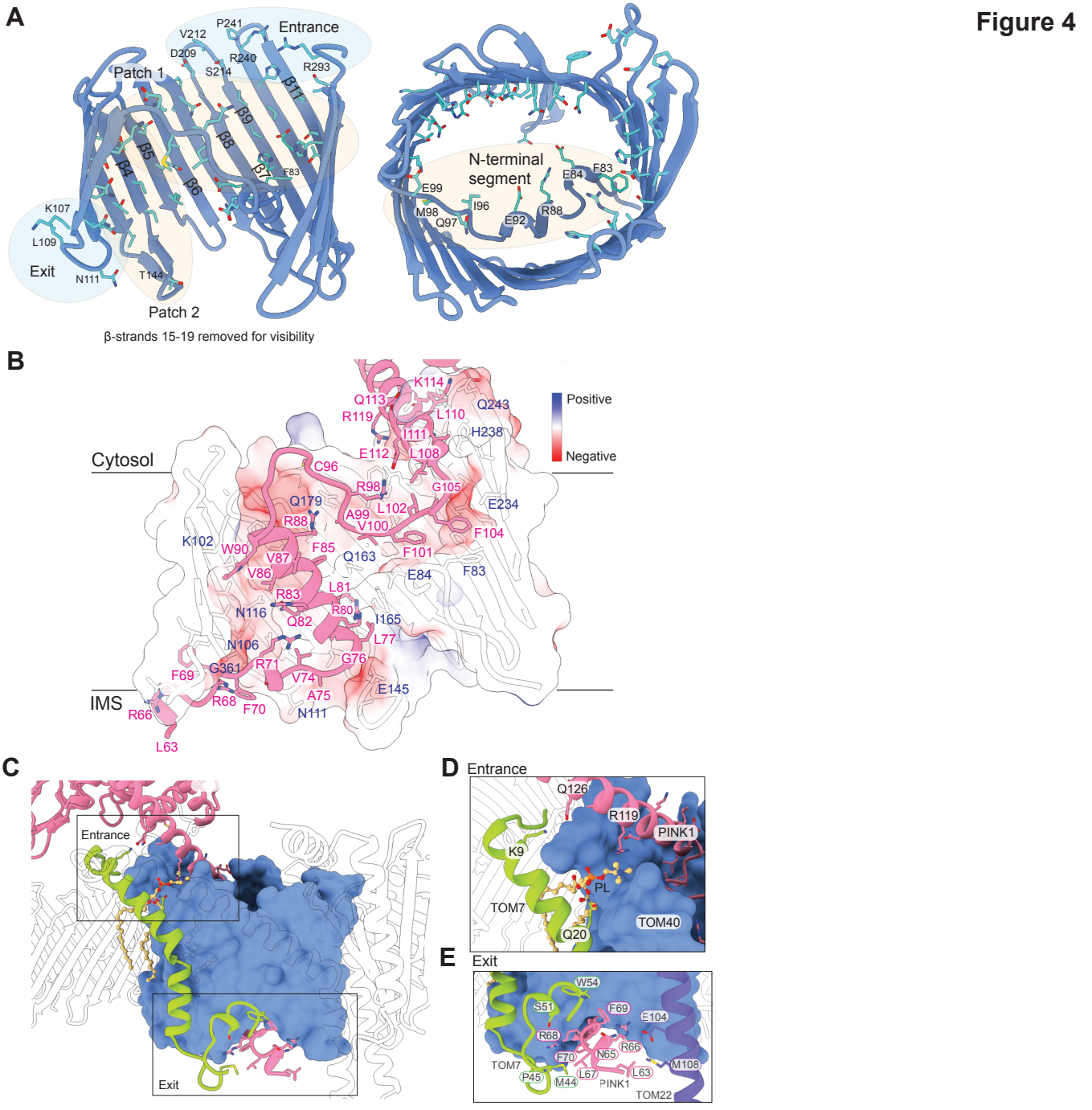
A
Entrance
P241
V212
D209
R240
S214
R293
Patch 1
β11
β9
β8
β5
β4
β6
β7
F83
K107
L109
Exit
N111
T144
Patch 2
β-strands 15-19 removed for visibility
N-terminal segment
E99
F83
E84
M98
I96
Q97
E92
R88
B
Cytosol
IMS
Positive
Negative
K114
Q113
R119
L110
Q243
I111
H238
E112
L108
C96
R98
G105
Q179
E234
R88
A99
L102
V100
F104
K102
W90
F85
F101
V87
Q163
E84
F83
V86
L81
R83
N116
R80
I165
Q82
L77
N106
R71
G76
F69
G361
V74
E145
A75
R68
F70
N111
R66
L63
C
Entrance
Exit
D
Entrance
Q126
R119
PINK1
K9
PL
TOM7
TOM40
Q20
E
Exit
W54
S51
F69
E104
R68
R66
N65
TOM7
F70
M108
P45
M44
L67
L63
PINK1
TOM22

Figure 5

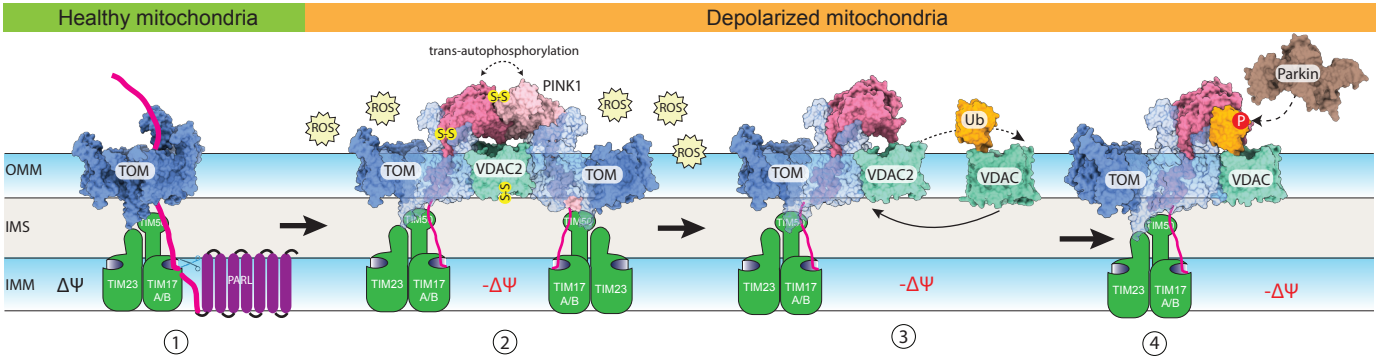
Healthy mitochondria
Depolarized mitochondria
trans-autophosphorylation
PINK1
S-S
ROS
OMM
IMS
IMM
ΔΨ
TOM
TIM50
TIM23
TIM17 A/B
PARL
VDAC2
VDAC
Ub
Parkin
P
-ΔΨ
1
2
3
4

Science
AAAS

Supplementary Materials for

Structure of human PINK1 at a mitochondrial TOM-VDAC array

Sylvie Callegari[1,2*], Nicholas S Kirk[1,2], Zhong Yan Gan[1,2], Toby Dite[1,2], Simon A Cobbold[1,2], Andrew Leis[1,2], Laura F Dagley[1,2], Alisa Glukhova[1,2,3,4,5*] and David Komander[1,2*]

Corresponding author: callegari.s@wehi.edu.au, glukhova.a@wehi.edu.au, dk@wehi.edu.au

The PDF file includes:

Materials and Methods
Supplementary Text
Figs. S1 to S15
Tables S1 to S2

Other Supplementary Materials for this manuscript include the following:

Data S1 to S2

Materials and Methods

Plasmids

The DNA sequence encoding full length human PINK1 with a C-terminal 3×FLAG tag was ordered as a gBlock gene fragment (Integrated DNA Technologies, Singapore) and cloned into the BamHI site of the pcDNA™5/FRT/TO vector (Invitrogen) using in-fusion cloning (Takara Bio). Cells were routinely checked for mycoplasma contamination using the MycoAlert Mycoplasma Detection Kit (Lonza).

Cell culture and transfection

Expi293F™ Cells (ThermoFisher) were cultured in Erlenmeyer flasks (Corning) containing Expi293™ expression medium (Gibco) according to the manufacturer's instructions. Cells were maintained at 37 ºC, 8% CO_2 in an orbital shaking incubator (Infors HT Minitron) set to 100 rpm.

For cryo-EM preparations, cell cultures were upscaled to 9 L, split across large 3 L Erlenmeyer flasks (Corning). When cell density reached 4.5 - 5.5x10^6 cells/mL, cells were diluted to a density of 3x10^6 cells/mL and transfected with the PINK1^{FLAG} plasmid to a final concentration of 1 μg/mL. Transfection was performed as previously described (*73*) using polyethyleneimine (PEI) MAX MW40000 (Polysciences), prepared as a 1 mg/mL stock solution in PBS, pH 7.0. Briefly, 9 mg plasmid was diluted in 900 mL Opti-MEM™ (Gibco) and PEI MAX was added (50 μg/mL), stirred gently to mix and incubated for 15 min at room temperature. The transfection solution was then added gently to cell cultures. At 18 h post transfection, cells were treated with 5 mM valproic acid (Sigma), 6.5 mM sodium proprionate (Sigma) and 0.9% glucose (w/v) to enhance protein expression. At 3 days post-transfection, cultures were treated with 10 μM oligomycin and 4 μM antimycin A (OA) for 3 h to depolarize mitochondrial membrane potential and accumulate PINK1. Cultures were then harvested by centrifugation at 1000×g.

Mitochondrial isolation

Harvested cells were washed in cold mitochondrial isolation buffer (75 mM mannitol, 225 mM sucrose, 10 mM MOPS (pH 7.2), 1 mM EGTA), before being resuspended in cold hypotonic buffer (100 mM sucrose, 10 mM MOPS (pH 7.2), 1 mM EGTA, 2 mM PMSF, 1x cOmplete Mini EDTA-free Protease Inhibitor Cocktail (Roche)) for 10 min (5 ml buffer/g cells) to osmotically swell the cells to facilitate disruption. Cells were subsequently homogenized on ice in a glass Potter-Elvehjem for 30 strokes using a PTFE pestle attached to a mechanical homogenizer (Glas-Col). 1 ml cold hypertonic buffer (1.25 M sucrose, 10 mM MOPS (pH 7.2)) was added to 5 ml homogenized cells before the total volume was doubled with isolation buffer. Unbroken cells, cell debris and nuclei were cleared by two rounds of centrifugation at 1000×g for 10 min. The supernatant containing the mitochondria was retained and mitochondria were collected by further centrifugation at 10,000×g. The mitochondrial pellet was washed in cold isolation buffer before a final centrifugation at 10,000×g. The mitochondrial pellet was then resuspended in isolation buffer and a bicinchoninic (BCA) assay (Pierce) was performed to determine total protein concentration.

Purification of PINK1 complex

Large scale purification of PINK1^{3xFLAG} containing complexes from mitochondria was based on a previously described protocol for purification of mitochondrial translocases (*74*). Mitochondria

were solubilized in solubilization buffer (1% (w/v) digitonin, 50 mM Tris/HCl (pH 7.4), 150 mM NaCl, 1 mM EDTA, 10% (w/v) glycerol, 1 mM PMSF, 1x cOmplete Mini EDTA-free Protease Inhibitor Cocktail (Roche), 5 µg/mL RNase A (Thermo Fisher)) at a ratio of 1 mg/mL and incubated for 30 min at 4°C with gentle stirring. Solubilized mitochondria were centrifuged at 14,000×g for 10 min at 4°C to pellet unsolubilized mitochondria. The supernatant was then added to anti-FLAG agarose affinity resin (Sigma) and incubated for 1 h at 4°C with gentle stirring. The solution was transferred to a gravity flow column to remove the unbound lysate. The anti-FLAG resin was washed with 15 column volumes (CV) of wash buffer containing digitonin (0.3% (w/v) digitonin, 50 mM Tris/HCl (pH 7.4), 150mM NaCl, 1 mM EDTA, 10% (w/v) glycerol), followed by 15 CV wash buffer containing glyco-diosgenin (GDN, Sigma) (0.05% (w/v) GDN, 50 mM Tris/HCl (pH 7.4), 150 mM NaCl, 1 mM EDTA, 10% (w/v) glycerol). Bound $PINK1^{FLAG}$ complexes were eluted by incubating the anti-FLAG resin in the gravity flow column with 250 µg/mL FLAG peptide (Sigma) in elution buffer (0.005% (w/v) GDN, 50 mM Tris/HCl (pH 7.4), 150 mM NaCl, 1 mM EDTA, 3% (w/v) glycerol) for 30 min at 4°C on a roller shaker. The elution was collected via gravity flow.

The eluate was concentrated using 100 kDa MWCO Amicon Ultra (Merck Millipore) and the PINK1-TOM-TIM23 complex was further purified via size exclusion chromatography using a Superose™ 6 Increase 3.2/300 column (Cytiva), equilibrated in 0.005% (w/v) GDN, 50 mM Tris/HCl (pH 7.4), 150 mM NaCl, 1 mM EDTA, 3% (w/v) glycerol, 1 mM DTT. Peak fractions were assessed by gel electrophoresis on reducing NuPAGE 4-12% Bis-Tris gels (Invitrogen), followed by gel staining with InstantBlue Coomassie Protein Stain (Abcam). Fractions containing PINK1-TOM-TIM23 components were pooled and concentrated using 100 kDa MWCO Amicon Ultra centrifugal filters. Protein concentration was measured using the BCA assay (Pierce).

Ubiquitin phosphorylation assays

Ubiquitin phosphorylation assays were carried using 0.5 µg/µl purified human PINK1-TOM-TIM23 and 15 µM ubiquitin in 50 mM Tris/HCl (pH 7.4), 50 mM KCl, 2.5 mM $MgCl_2$, 1 mM DTT. Reactions were initiated by the addition of 1 mM ATP (Sigma) and incubated at 22 °C for the timepoints indicated. Reactions were quenched in SDS sample buffer (66 mM Tris/HCl (pH 6.8), 2% (w/v) SDS, 10% (v/v) glycerol, 0.005% (w/v) bromophenol blue), and boiled at 95°C for 10 min.

Western blotting

Samples in SDS sample buffer were separated on reducing NuPAGE 4-12% Bis-Tris gels (Invitrogen). Protein transfer was carried out using the Trans-Blot Turbo Transfer System (Bio-Rad) onto PVDF membranes. Membranes were then blocked in 5% (w/v) skim milk powder in Tris-buffered saline containing 0.1% Tween-20 (TBS-T) and incubated with primary antibodies in TBS-T overnight at 4 °C. Membranes were washed in TBS-T, incubated in secondary antibody for ~1 h, then washed in TBS-T prior to incubation in Clarity Western ECL Substrate (Bio-Rad) and detection using a ChemiDoc (Bio-Rad). Primary antibodies used were rabbit anti-PINK1 D8G3 (Cell Signaling Technology, #6946), rabbit anti-phospho-ubiquitin (Ser65) E2J6T (Cell Signaling Technology, #62802), Mouse anti-Ubi-1 (Novus Biologicals, #NB300-130), rabbit anti-TOM20 (Proteintech, #11802-1-AP), rabbit anti-TOM22 (Proteintech, #11278-1-AP), rabbit anti-TIM23 (Proteintech, #11123-1-AP), rabbit anti-TIM50 (Proteintech, #22229-1-AP),

rabbit anti-TIM44 (Proteintech, #13859-1-AP), rabbit anti-ATP5B (kind gift from Peter Rehling, Göttingen, Germany)(*75*). Secondary antibodies used are goat anti-rabbit HRP-conjugated (SouthernBiotech, #4010-05) and goat anti-mouse HRP-conjugated (SouthernBiotech, #1030-05).

Sulfo-SDA crosslinking

Purified PINK1-TOM-TIM23 complex was buffer exchanged into cross-linking buffer (50 mM HEPES (pH 7.4), 150 mM NaCl, 0.005% (w/v) GDN) using a 100 kDa MWCO Amicon Ultra centrifugal filter. Sulfo-NHS-diazirine (Sulfo-SDA, Thermo Fisher) was prepared as a 1 mg/mL 2X stock and added to an equal volume of 2 µg/µl PINK1-TOM-TIM23 complex. Samples were incubated for 2 h at 4°C before UV activation of the crosslinker by irradiating at 1000 kV using a UV lamp for 2 min. The reaction was quenched by adding ammonium bicarbonate to a final concentration of 50 mM and incubating for 15 min on ice. The sample was subsequently processed for mass spectrometry analysis.

In gel digest of SDS-PAGE proteins for mass spectrometry analysis

Gel bands of interest were excised from an SDS-PAGE gel and transferred to fresh 1.5 mL centrifuge tubes. A volume of 100 µL of 50% (v/v) acetonitrile (ACN), 50 mM ammonium bicarbonate (AmBic) was added to each band and allowed to destain at 37 ºC with shaking for 15 min. This step was repeated until gel bands were clear, before dehydrating the gel bands with 100% (v/v) ACN for 5 min. Gel bands were rehydrated in 100 µL of 50 mM AmBic containing 10 mM dithiothreitol (DTT) and allowed to reduce at 37 ºC for 30 min, then alkylated with 55 mM iodoacetamide for 30 min in the dark. Excess solution was removed via vacuum trap and gel bands were washed twice with 100 µL of 50% (v/v) ACN, 50 mM AmBic prior to dehydration with 100% ACN (v/v) for 5 min. A volume of 40 µL of trypsin (Sigma, EMS0004) (15 ng/µL in 25 mM AmBic) was added to each gel band and allowed to rehydrate at 4 ºC for 45 min prior to overnight digestion at 37 ºC. The following day, peptides were extracted using a solution of 60% ACN (v/v) and 0.1% (v/v) formic acid (FA). The collected peptides were subsequently lyophilized to dryness using a CentriVap (Labconco) and reconstituted in 25 µL 0.1% (v/v) FA and 2% (v/v) ACN ready for MS analysis.

In-solution enzymatic digestion of cross-linked mass-spectrometry samples

Proteins were incubated with 50 mM AmBic, 8 M Urea and 1 mM DTT for 30 min at 37 ºC. Proteins were alkylated using 10 mM iodoacetamide for 1 h in the dark, after which reactions were quenched with 10 mM DTT. Samples were diluted with 50 mM AmBic to reduce Urea to 1 M concentration. A volume equivalent to 1 µg trypsin was added for overnight digestion at 37 ºC. Peptides were then desalted using C18 STAGE tips containing 2X Empore C18 resin plugs (Empore, 2215) and collected into new centrifuge tubes by centrifugation. The collected peptides were lyophilized to dryness using a CentriVap (Labconco).

High pH fractionation of crosslinked peptides on STAGE tips

C18 STAGE tips (as described above) were prepared by equilibrating with 100% (v/v) ACN, followed by 25 mM ammonium formate (pH 10), 50% (v/v) ACN, then finally 25 mM ammonium formate (pH 10). Peptides were resuspended in 25 mM ammonium formate (pH 10) and loaded onto STAGE tips. STAGE tips were washed twice with 25 mM ammonium formate (pH 10). Peptides were then eluted into 7 fractions in 40 µl volumes using 25 mM ammonium

formate (pH 10) and ACN in increasing ACN concentrations from 5%, 7.5%, 10%, 12.5%, 15%, 17.5% and finally 50% (v/v). Fractions were concatenated (fraction 1: 5% + 12.5% + 50%), (fraction 2: 7.5% + 15%), (fraction 3: 10% + 17.5%). The concatenated fractions were subsequently lyophilized to dryness using a CentriVap (Labconco) and reconstituted in 0.1% formic acid (v/v) and 2% (v/v) ACN ready for MS analysis.

Mass spectrometry analysis

For the proteins excised from SDS-PAGE, reconstituted peptides were separated by reverse-phase chromatography on a C_{18} fused silica column (inner diameter 75 µm, OD 360 µm × 15 cm length, 1.6 µm C18 beads) packed into an emitter tip (IonOpticks), using a custom nano-flow HPLC (Thermo Ultimate 300 RSLC Nano-LC with a PAL systems CTC autosampler). The HPLC was coupled to a timsTOF Pro (Bruker) equipped with a CaptiveSpray source. Peptides were loaded directly onto the column at a constant flow rate of 400 nL/min with buffer A (99.9% Milli-Q water, 0.1% FA) and eluted with a 30-min linear gradient from 2 to 34% buffer B (99.9% ACN, 0.1% FA). The timsTOF Pro was operated in PASEF mode using Compass Hystar 6.2.1. Settings were as follows: Mass Range 100 to 1700 m/z, 1/K0 Start 0.6 V·s/cm^2 End 1.6 V·s/cm^2, Ramp time 110.1 ms, Lock Duty Cycle to 100%, Capillary Voltage 1600V, Dry Gas 3 l/min, Dry Temp 180 °C, PASEF settings: 10 MS/MS scans (total cycle time 1.27 sec), charge range 0-5, active exclusion for 0.4 min, Scheduling Target intensity 10000, Intensity threshold 2500, CID collision energy 42 eV.

For the crosslinking MS samples, reconstituted peptides were analyzed on an Orbitrap Eclipse Tribrid mass spectrometer (Thermo Fisher) that was interfaced with Neo Vanquish liquid chromatography system. Peptides were loaded onto a 15cm IonOpticks column (inner diameter 75 µm, OD 360 µm, 1.6 µm C18 beads) using pressure-controlled loading with a maximum pressure of 1,500 bar. A linear gradient of 3% to 30% of solvent B was employed at 400 nL/min flow rate (solvent B: 99% (v/v) ACN) for 100 min, followed by 30% to 40% solvent B for 20 min, followed by 35% to 99% solvent B for 5 min, followed by 90% B for 10 min, and final wash at 3% solvent B for 10 min, comprising a total of 145 min run with a 120 min gradient. Data was acquired in a data dependent acquisition (DDA) mode. MS1 spectra were acquired in the Orbitrap (R = 120k; normalized AGC target = standard; MaxIT = Auto; RF Lens = 30%; scan range = 380-1400; profile data). Dynamic exclusion was employed for 30 s excluding all charge states for a given precursor. Data dependent MS2 spectra were collected in the Orbitrap for precursors with charge states 3-8 (R = 50k; HCD collision energy mode = assisted; normalized HCD collision energies = 25%, 30%; scan range mode = normal; normalized AGC target = 200%; MaxIT = 150 ms).

Mass spectrometry raw data processing and analysis

For the in-gel digests, raw MS data were searched using MaxQuant 1.6.17.0 incorporating the Andromeda search engine(*76*). The analysis was conducted against the Human proteome FASTA database obtained from UniProt in May 2021. Variable modifications included protein N-terminal acetylation, methionine oxidation, while cysteine carbamidomethylation was selected as a fixed modification. Trypsin served as the specified enzyme for digestion, with an allowance for up to two missed cleavages. To ensure high confidence in the results, the false discovery rate (FDR) was set at 1% for both proteins and peptides. A peptide tolerance of 4.5 ppm was used during main search.

For the crosslinking samples, raw data files were converted to MGF files using MS convert (*77*). MGF files were searched against a FASTA file containing the list of proteins identified from in gel digest using XiSearch software (*78*)(version 1.7.6.7) with the following settings: crosslinker = multiple, SDA and noncovalent; fixed modifications = Carbamidomethylation (C); variable modifications = oxidation (M), sda-loop (KSTY) DELTAMASS:82.04186484, sda-hydro (KSTY) DELTAMASS:100.052430; MS1 tolerance = 6.0ppm, MS2 tolerance = 20.0ppm; losses = H_2O,NH_3, CH_3SOH, CleavableCrossLinkerPeptide:MASS:82.04186484). FDR was performed with the in-built xiFDR set to 5%. Data were visualized using the XiView software (*79*)(*61*)(*62*)(*63*).

Cryo-EM sample preparation and data collection

UltrAuFoil R1.2/1.3 grids (Quantifoil) were plasma cleaned using a Henniker Plasma HPT-200 operated at 50% power for 3 min. Sample (4 µL of a 4 mg/mL protein complex sample) was applied to grids in a VitroBot Mark IV (TFS) at 4 °C and 90% humidity, blotted at blot force 10 for 2 s and vitrified in liquid ethane.

Data were collected on a Titan Krios G4 (ThermoFisher Scientific) equipped with a Gatan K3 camera and a Quantum-GIF energy filter. EPU 3 software was used to automate data collection. Imaging was performed in nanoprobe energy filtered zero loss mode using a 10 eV slit width. A nominal magnification of 105,000 × was used, giving a calibrated specimen level pixel size of 0.833 Å. A C2 condenser aperture of 50 µm and objective aperture of 70 µm were used and the K3 camera was operated in correlated double sampling mode at a dose rate of 10.9 e^{-}.$pixel^{-1}$ s^{-1}. Movies were collected using a 3.34 s exposure time fractionated into 50 sub-frames resulting in a total accumulated dose of 52.4 e^{-} $Å^{-2}$ per movie. 16,992 movies were collected in faster acquisition mode (AFIS) at a defocus range of -0.5 µm to -2.0 µm in two sessions from two grids.

Cryo-EM refinement and model building

All processing was performed within cryoSPARC v4.5.1-3 (*80*) . 16,992 movies were imported, patch-motion corrected and patch-CTF estimation was performed. Micrographs containing thick or contaminating ice, CTF fit resolution > 4 Å or high motion statistics were removed, leaving 15,960 good micrographs. Particles were picked using templates generated from a low-resolution structure of the PINK1-TOM complex from an earlier screening dataset and extracted, binned 6X (box size 112 px). Particles were 2D classified, with obvious non-protein particles and duplicates removed. Heterogeneous refinement using the screening reconstruction and two decoy models was performed. Particles corresponding to the PINK1-TOM complex were re-extracted binned 2x (box size 336 px) and iteratively heterogeneous refined to remove remaining bad particles. Remaining particles were aligned to the C2 axis and duplicates removed, leaving 850k particles. Good particles were re-extracted with a pixel size of 1.272 (440 px box) and refined in C2 symmetry with symmetry relaxation using the NU-refine job to give the consensus 3.3 Å map. 3D classification without alignment was used, with a soft mask covering the PINK1-TOM20 portion of the map. Classes containing intact PINK1 and TOM20 were combined and locally refined. CTF refinement and reference-based motion refinement were performed before another local refinement. 3D classification without alignment into 8 classes was performed using a soft mask covering the VDAC dimer. One class containing poor density was removed and the

remaining particles locally refined again without symmetry, resulting in a 3.1 Å map containing the entire TOM-VDAC complex (‘overall complex’ map).

Symmetry expansion in C2 was used on the particles from the consensus 3.3 Å map, followed by local refinement with a soft mask covering the asymmetric unit (1x VDAC2, 1x PINK1, 1x TOM20, 1x TOM core), resulting in a 2.75 Å map (‘symexp’ map). From the symmetry expanded particles, a soft mask covering TOM20 plus the TOM22 membrane anchor region on one asymmetric unit was generated and 3D variability was performed with 3 modes, filtered to 5 Å. The results were clustered into 6 classes and the class with the most complete TOM20 was locally refined to give the third map (‘long TOM20’ map).

Molecular modelling was performed on the overall complex with no symmetry, adjustments were made from this model to fit the ‘SymExp’ and ‘long TOM20’ maps. AlphaFold3 (*81*) was used to generate initial atomic coordinates for the PINK1-TOM20 dimer and VDAC2. Two copies of the TOM core complex were initiated from PDB 7CP9. ChimeraX v1.7 (*82*) was used to remove disordered loops, rigid body fit the models and combine the coordinates into a single file. The models were then morphed to fit the density with adaptive restraints to the initial models using ISOLDE v1.7 (*83*) . Restraints were released and the coordinates refined within ISOLDE v1.7 and 1.8. Missing residues were modelled into density using COOT v0.9.8.93 (*84*) . Lipids were modelled as PC as per PDB 7CP9, with lipid tails falling outside density set to 0 occupancy. Lipids with poor density for the headgroup were omitted. Final real space refinement was performed using PHENIX v1.21.1 (*85*) with reference and Ramachandran restraints activated. Cryo-EM data collection and refinement statistics are provided in **Table S2.**

Supplementary Text

Modelling of the VDAC2 dimer

Multiple observations prompted us to model a VDAC2 homodimer as the central pore dimer in our structure. An additional TOM dimer could be excluded for lack of small TOM subunits, an unlikely dimer interface between barrels, and location and conformation of the N-terminal helix inside the barrel. VDAC channels are evolutionarily related to TOM40, have a similar β-barrel topology and are abundant MOM proteins (*86*). With MS evidence for all three VDAC channels (**Fig. 1C, Table S1**), all combinations of possible homo and heterodimers with VDAC1, -2 and -3 were modelled into the density (**fig. S7**). Several features were consistent only with a VDAC2 dimer. Most notable were tight interactions and cryoEM density consistent with symmetric disulfide bonds between Cys47 in the IMS exposed β1-2 loop with Cys76 in the IMS exposed β3-4 loop on the neighbouring VDAC channels (**Fig. 2D, fig. S7B**); these Cys residues are conserved in VDAC2 and VDAC3, but not VDAC1. Interestingly, these Cys residues in VDAC2 are modified by succination in a mouse model of Leigh syndrome, a mitochondrial disease (*87*), but have not previously been implicated in protein interactions. Secondly, aromatic residues at +2 and -1 from Cys76 on the β3-4 loop, visible as bulky residues in the density map, are only present in VDAC1 and VDAC2, excluding VDAC3. Furthermore, aromatic residues on β16-17 and β19 that are exclusive to VDAC1 and VDAC3 would be too bulky to fit into the corresponding smaller densities on the cryoEM map (**fig. S7C**). Finally, residues of the unique VDAC2 N-terminal extension were observed in some classes (**fig. S7A**). While there may be a mix of species present within the dataset, veiled by heterogeneity, we have chosen to model a VDAC2 homodimer as this is the only species that fits each of the observations.

Comparison of Apo-TOM40 and associated small TOMs with the PINK1-trapped TOM40 unit

To ascertain whether there are structural alterations to the TOM40 barrel, or surrounding subunits, upon pre-sequence translocation. We compared the apo-TOM40 barrel from our structure with the PINK1-containing TOM40 barrel (**fig. S13A-D**) and calculated the root mean square deviation (RMSD) of the αC atoms to assess structural variability (**fig. S13E**). A clear displacement of the glutamine rich patch on the TOM40 N-extension can be observed in the PINK1-containing barrel, resulting in a repositioning of TOM40 Phe83 which allows it to contact PINK1 Phe104. There are additional variations within the TOM40 cytosolic-facing entrance loops (β9-β10 and β11-β12) and the IMS facing β3-β4 loops at the exit region. In fact, in our reconstruction, there was strong density for the β3-β4 loops, suggesting structural organization. This prompted us to model these regions as β–sheets. Compared with previously published structures of TOM40 containing trapped sfGFP-tagged precursors in yeast (*69*, *88*) , human TOM40 appears to show greater structural rearrangement (**fig. S13E**). However, this could also be due to the nature of the trapped precursor.

Compared with the apo-TOM40 barrel, TOM7 undergoes a 6.5° pivot of its cytoplasmic helix (residues 7-25) to contact the PINK1 N-helix through a direct interaction between TOM7 Lys9 and PINK1 Gln126, as well as a phospholipid-mediated contact between PINK1 Arg119 and TOM7 Gln20 (**fig. S13F, Fig 4D**). A small shift in TOM5 could also be observed with the biggest difference being the TOM5 N-terminus, which could be resolved in association with PINK1, but not with the apo-TOM40 barrel, indicating that this region is flexible (**fig. S13F**). The positioning of TOM6, which makes the least contacts with PINK1, remains unaltered.

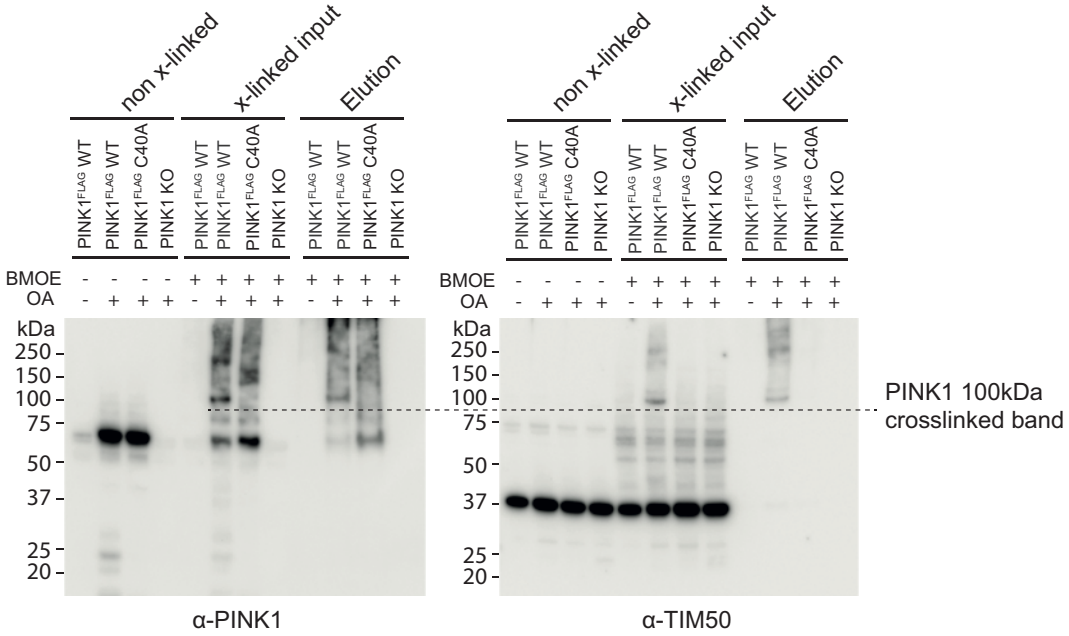

Fig. S1 The N-terminus of PINK1 crosslinks with TIM50.

Isolated mitochondria which had accumulated PINK1^{FLAG} were crosslinked using the cysteine reactive crosslinker Bismaleimidoethane (BMOE) and solubilised in SDS lysis buffer. Lysates were then diluted into a milder immunoprecipitation buffer containing Triton X-100 for immunoprecipitation using anti-FLAG resin. Crosslinked bands were visualised by running the elutions on a NuPAGE 4-12% Bis-Tris gel and blotting for PINK1, as well as for the candidate interactor, TIM50. The PINK1 C40A mutant was used as a non-crosslink forming control. The PINK1 100kDa crosslinked band is indicated. *N* = 2 independent experiments.

Fig. S1.
The N-terminus of PINK1 crosslinks with TIM50.

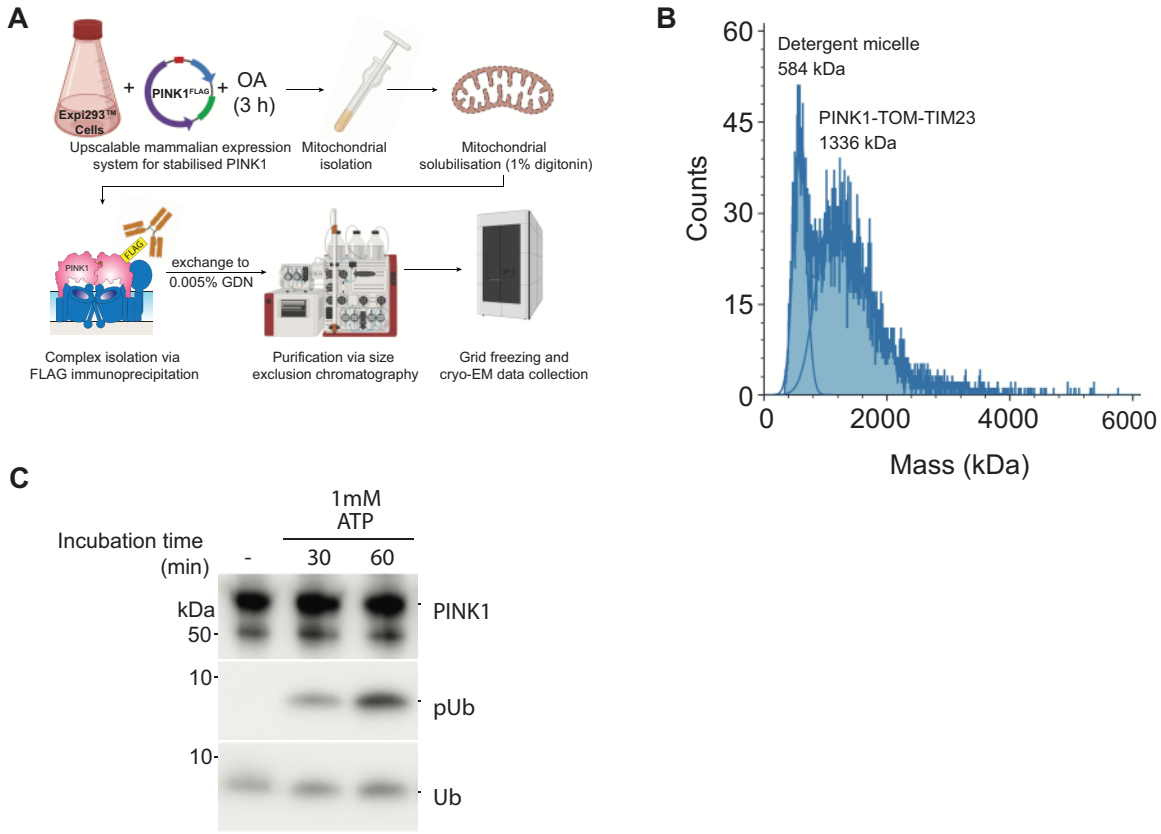

Fig. S2: Large scale purification of PINK1-TOM-TIM23.

(A) Schematic of workflow for large scale expression and purification of PINK1^{3XFLAG} complexes. OA: 10μM Oligomycin / 4μM Antimycin A. Figure was made using elements from Biorender.com.
(B) Mass photometry profile of purified PINK1-TOM-TIM23 complex. The mass of the complex is approximately 750kDa, calculated by subtracting the size of the detergent micelle from the isolated complex which is within a micelle. *N* = 3 technical replicates.
(C) PINK1 activity assay. Purified human PINK1 complex from (A) was incubated with ubiquitin and ATP for the indicated time period. Samples were loaded onto a NuPAGE 4-12% Bis-Tris gel, western blotted and probed for the indicated antibodies. *N* = 2 independent experiments.

Fig. S2.
Large scale purification of PINK1-TOM-TIM23.

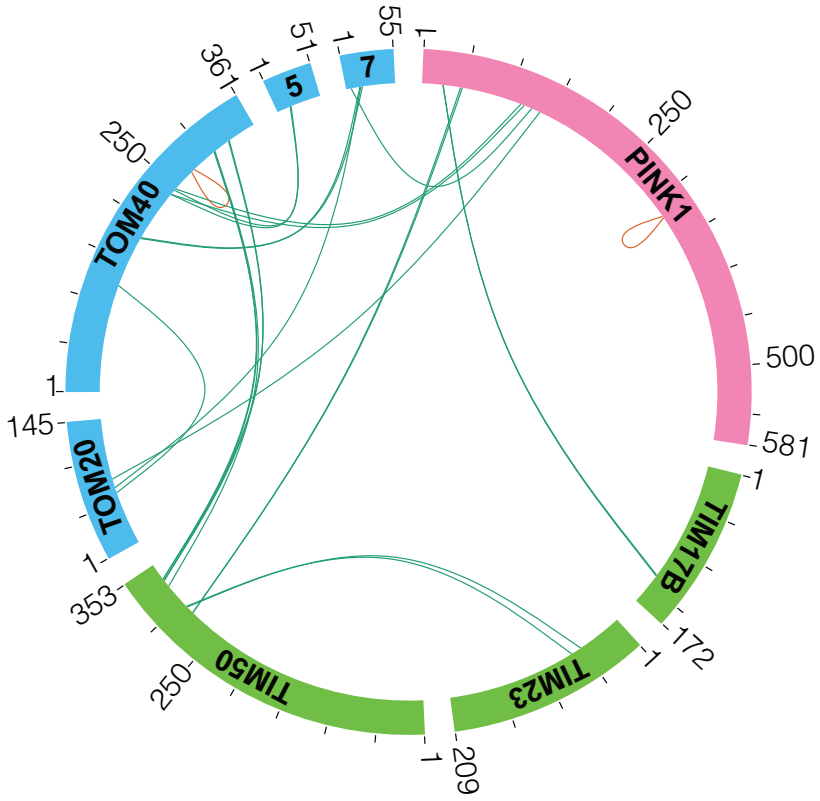

Fig. S3: XL-MS analysis of PINK1-TOM-TIM23 complex components

Purified PINK1-TOM-TIM23 complex was crosslinked using Sulfo-SDA. The crosslinked complex was digested and fractionated at high pH to enrich for crosslinked peptides. Peptides were analysed using LC-MS and crosslinked residues were searched using XiSearch. Map shows all inter-protein crosslinks identified between PINK1, TOM and TIM23 complex components (green loops), as well as links with overlapping peptides (possible oligomers) (orange loops) (Table S1 and data S2). Protein amino acid residues are shown on the outside of the circle. Map was generated using xiview. *N* = 2 independent experiments, but results shown are representative from 1 experiment.

Fig. S3.
XL-MS analysis of PINK1-TOM-TIM23 complex components.

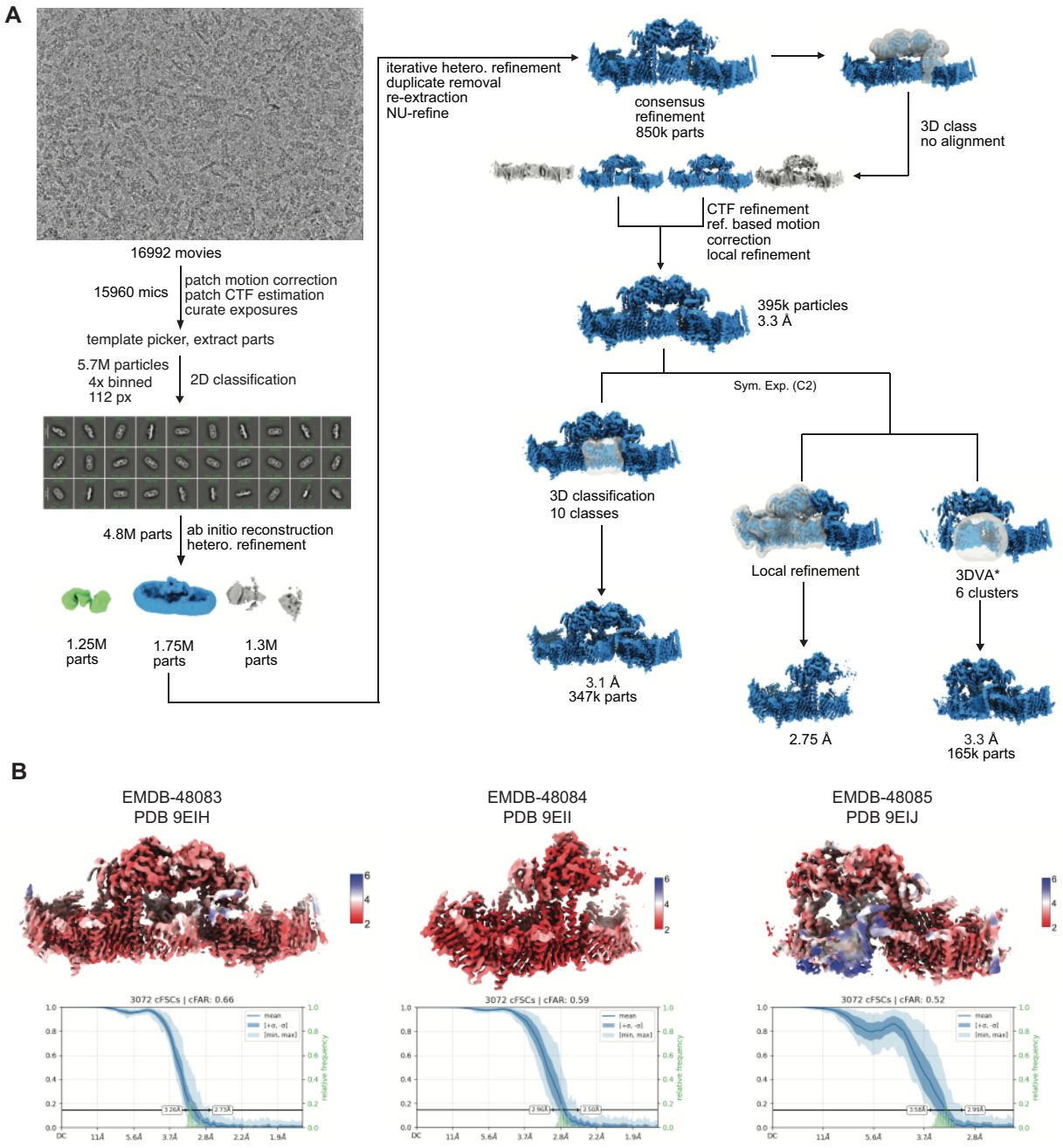

Fig. S4 CryoEM single particle analysis data processing.

(A) Flow chart for cryoEM analysis as described in methods.
(B) Local resolution maps, with resolution calculations.

Fig. S4.

CryoEM single particle analysis data processing.

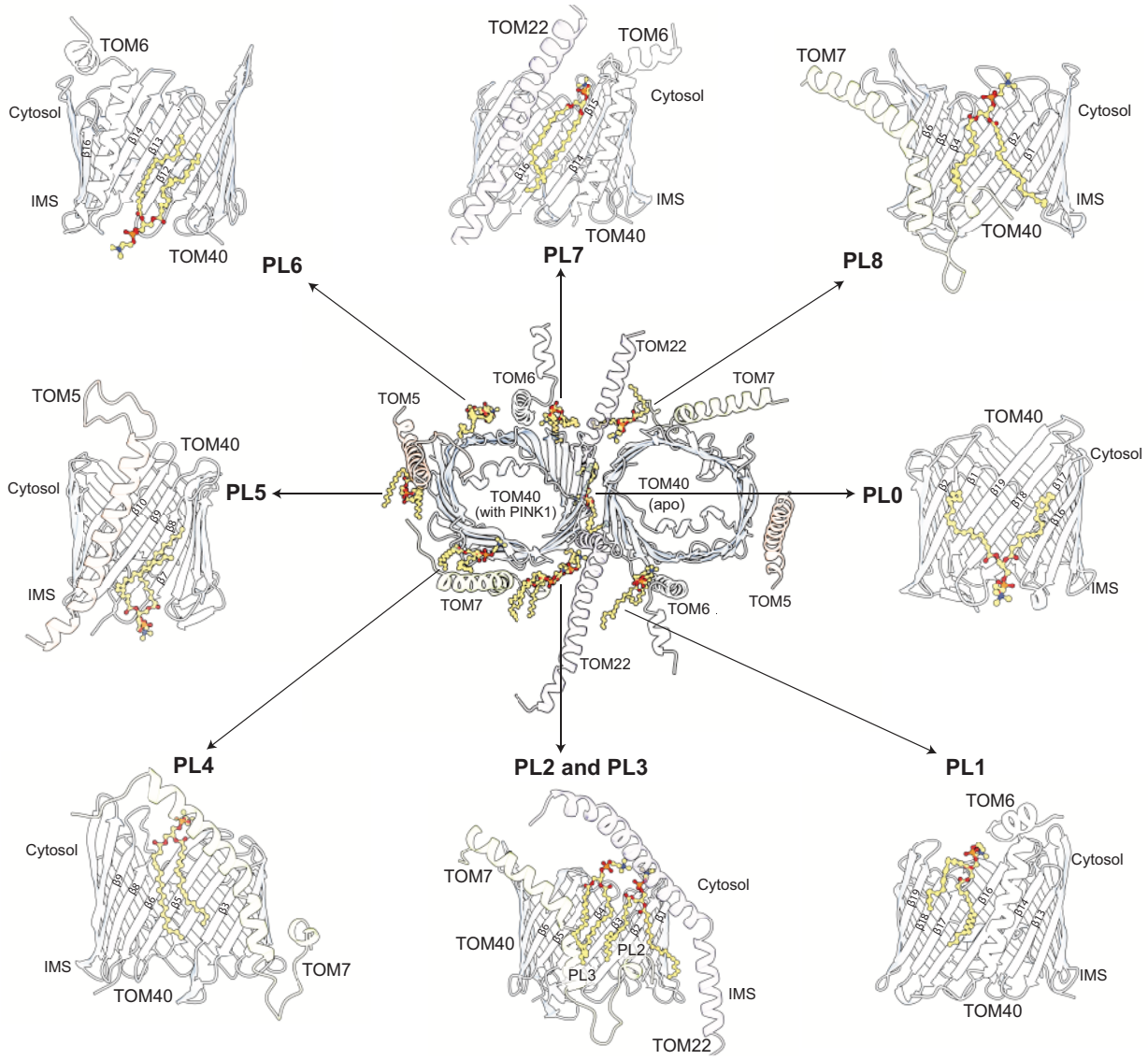

Fig. S5: Lipids surrounding the TOM core complex

Ribbon model of the asymmetric TOM core complex, as viewed from the cytosol, showing the surrounding phospholipids as coloured ball and stick models (middle). Around the periphery are individual views of each phospholipid on the TOM barrel, with neighboring TOM complex subunits. Each is viewed along the membrane plane.

Fig. S5.
Lipids surrounding the TOM core complex.

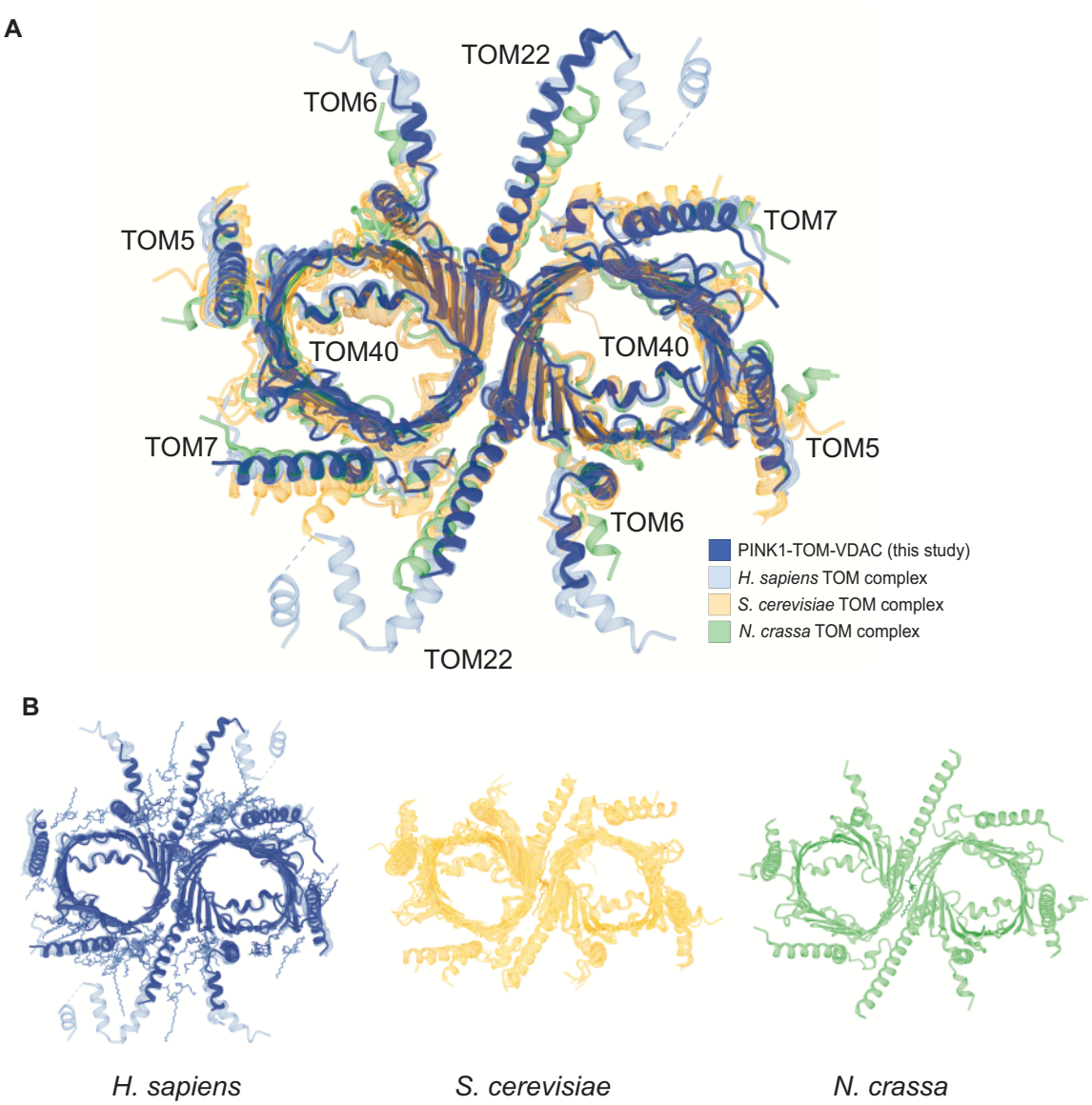

Fig. S6: Comparison of TOM structures across species

(A) Comparison of published TOM complex structures across species. Atomic models for each structure were aligned using the matchmaker function in ChimeraX. PDB numbers: *H. sapiens* 7CP9 *(41)*, 7VD2 *(38)*, 7CK6 *(40)*; *S. cerevisiae* 6UCU *(52)*, 6JNF *(53)*, 8HCO *(51)*, 8W5J *(69)*; *N. crassa* 8B4I *(46)*. **(B)** As in (A) but with models separated out into species. Lipids are shown as sticks.

Fig. S6.

Comparison of TOM structures across species.

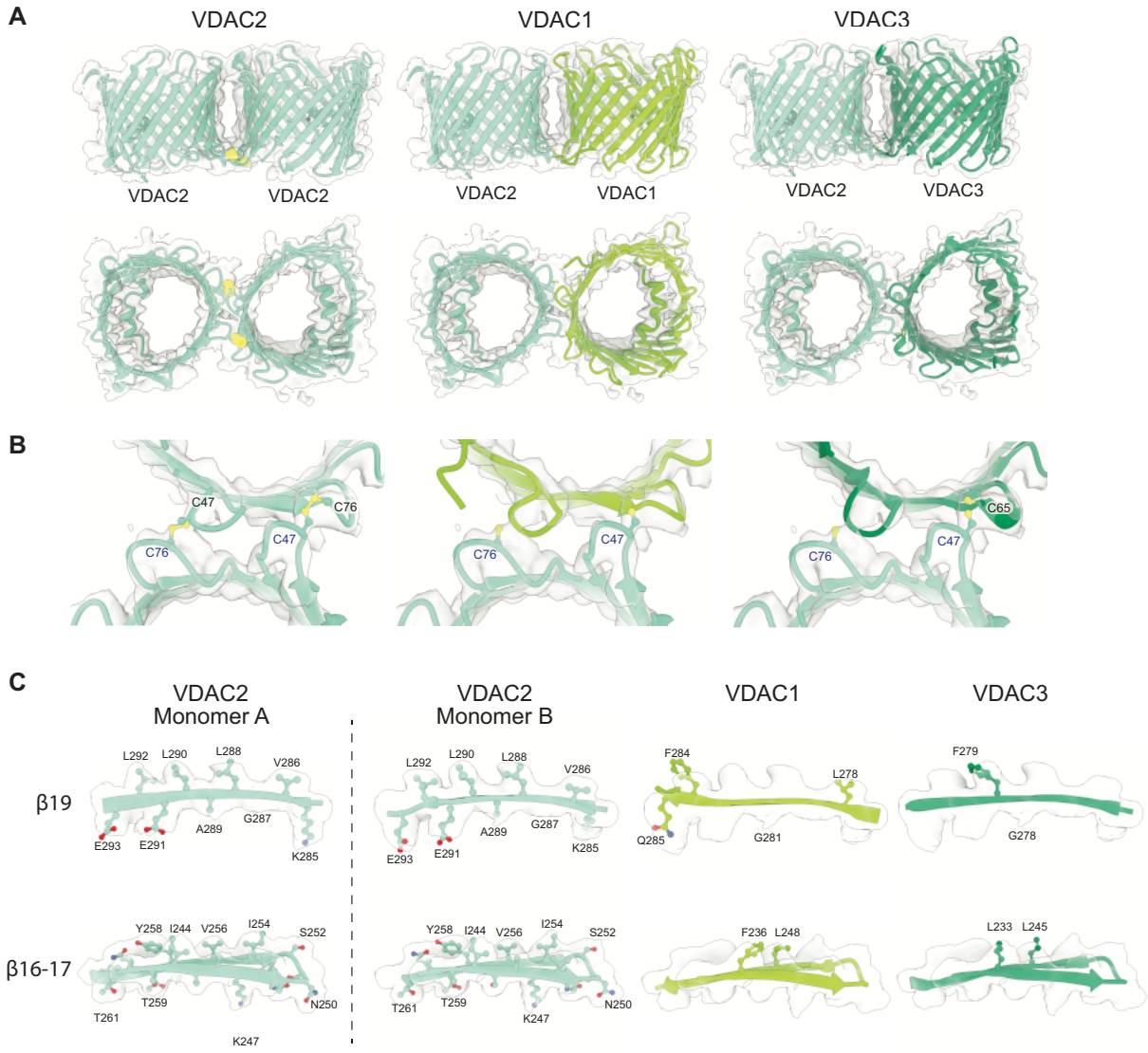

Fig. S7: Modelling of the VDAC2 dimer.

(A) To verify the identity of the VDAC2 dimer, the structure was processed using C1 symmetry and the three human VDAC isoforms were fitted. Side views along the membrane plane, and views from the IMS looking towards the cytosol are shown. The atomic model is superimposed on the cryo-EM density. **(B)** A close up view of the dimer interface after fitting of the VDAC isoforms. Cysteines are shown in yellow as ball and stick model. **(C)** A close up view of two regions in VDAC2 (β19 and β16-17) where differences in aromatic sidechains between VDAC isoforms support the identity of VDAC2. Only differing sidechains are shown for VDAC1 and VDAC3. The atomic model for VDAC1 and VDAC3 are superimposed on the cryo EM density of monomer B of VDAC2.

Fig. S7.
Modelling of the VDAC2 dimer.

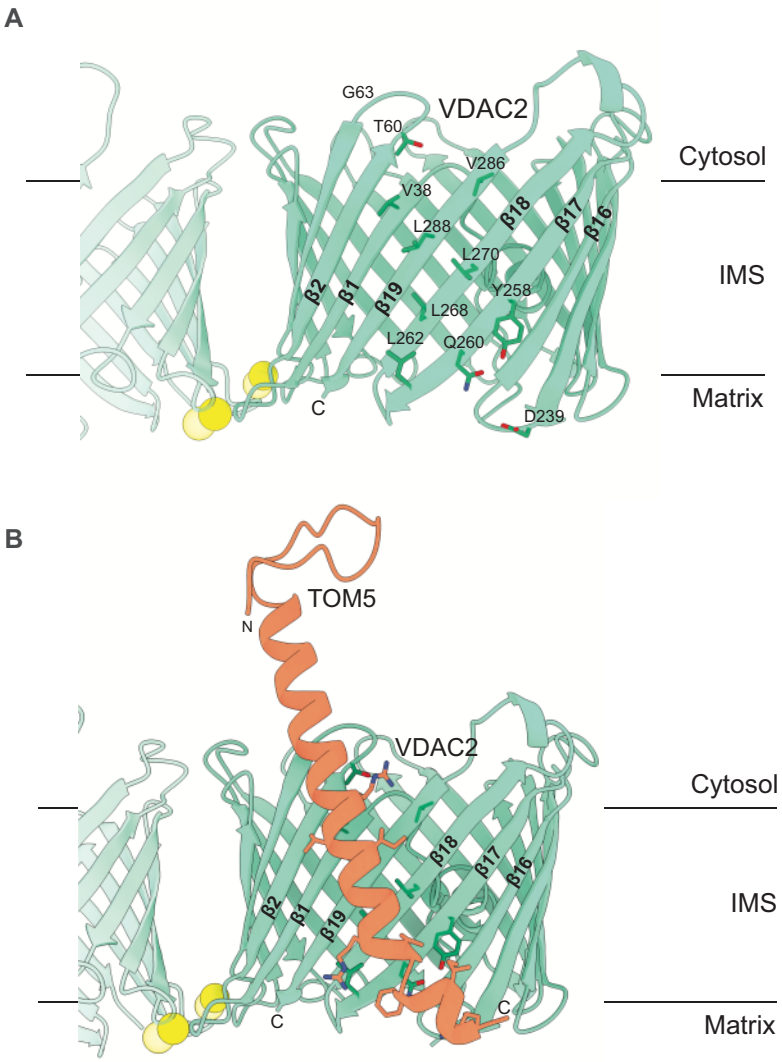

Fig. S8: VDAC2 association with TOM40 is mediated by TOM5.

(A) Model of the VDAC2 dimer, viewed along the membrane plane, showing the sidechains for residues that interact with TOM5. Disulfide bonds are indicated by yellow spheres. **(B)** As in (A) but with the addition of the model for TOM5.

Fig. S8.
VDAC association with TOM40 is mediated by TOM5.

Fig. S9: Multiple sequence alignment of human VDAC isoforms.

The three isoforms of human VDAC; VDAC1 (#P21796), VDAC2 (#P45880) and VDAC3 (#Q9Y277) were aligned using Clustal and the alignment visualized using Jalview. Beta-strands are indicated by blue boxes and numbered above the boxes, cysteines are highlighted in yellow and TOM5 interacting residues are highlighted in orange. A red star, denotes the cysteines that are IMS exposed and a red outline denotes C47 and C76, responsible for VDAC2 dimerization.

Fig. S9.

Multiple sequence alignment of human VDAC isoforms.

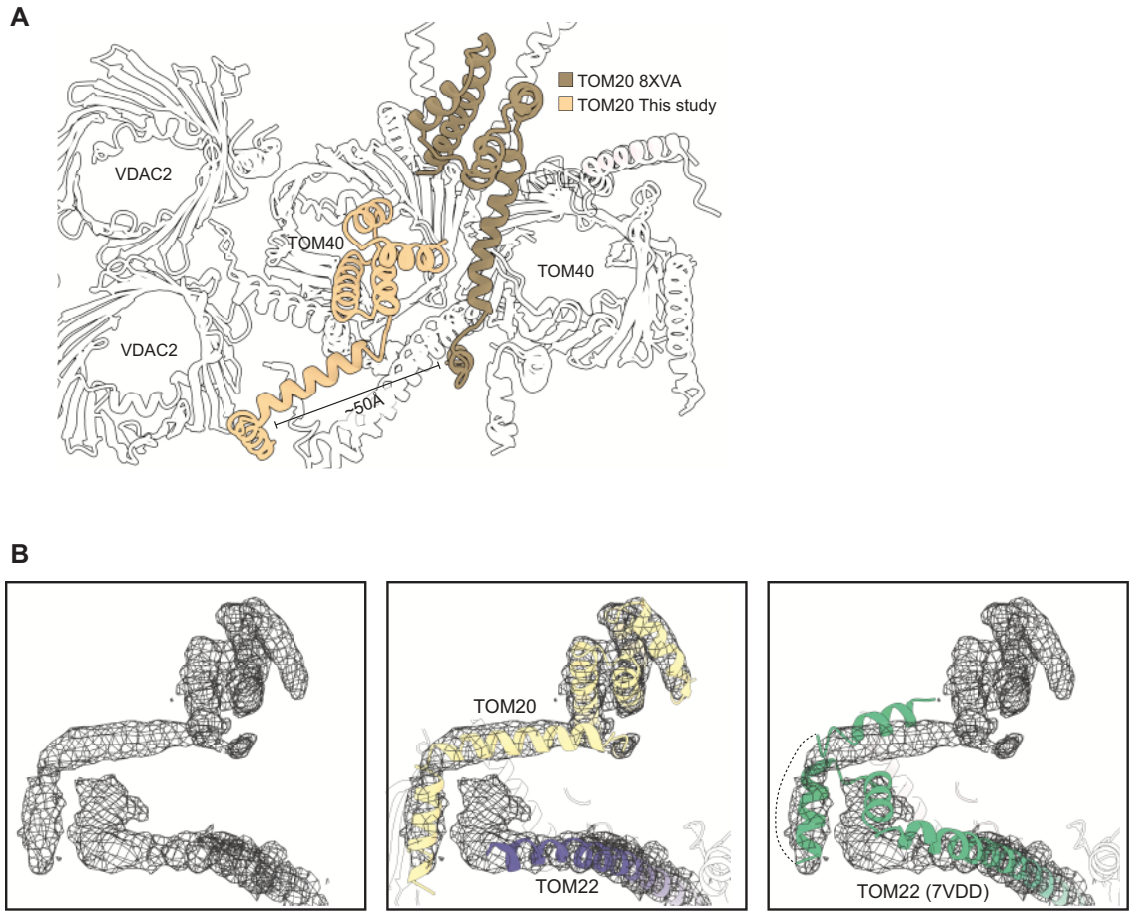

Fig. S10: TOM20 and TOM22 comparison with other published human TOM complex structures.

(A) The placement of the transmembrane helix of TOM20 within our atomic model of the TOM complex compared with the location of TOM20 in a previously published model of the crosslinked TOM complex (8XVA)*(39)*, superimposed on our model.
(B) Left panel; Our cryoEM density (represented in mesh) for regions that we assigned to TOM20 and the cytosolic portion of TOM22; middle panel; cryoEM density with our atomic model for TOM20 and TOM22 superimposed. right panel: our cryoEM density with the published atomic model for TOM22 (7VDD) *(38)* superimposed.

Fig. S10.
TOM20 and TOM22 comparison with other published human TOM complex structures.

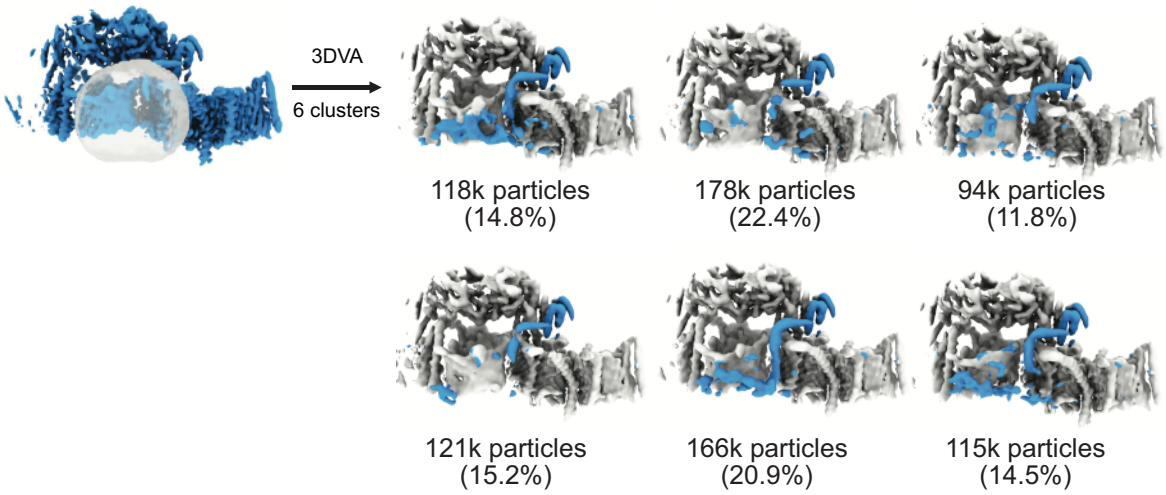

Fig. S11: Reconstructions of 3D variability clusters of the TOM20 N-terminal region.

The grey overlay on left is the mask used for 3DVA. Blue density on right represents density that is variable or corresponds to TOM20 from each cluster. The number of particles within each cluster and the percentage with respect to total particle number (795k) are noted above each cluster.

Fig. S11.

Reconstructions of 3D variability clusters of the TOM20 N-terminal region.

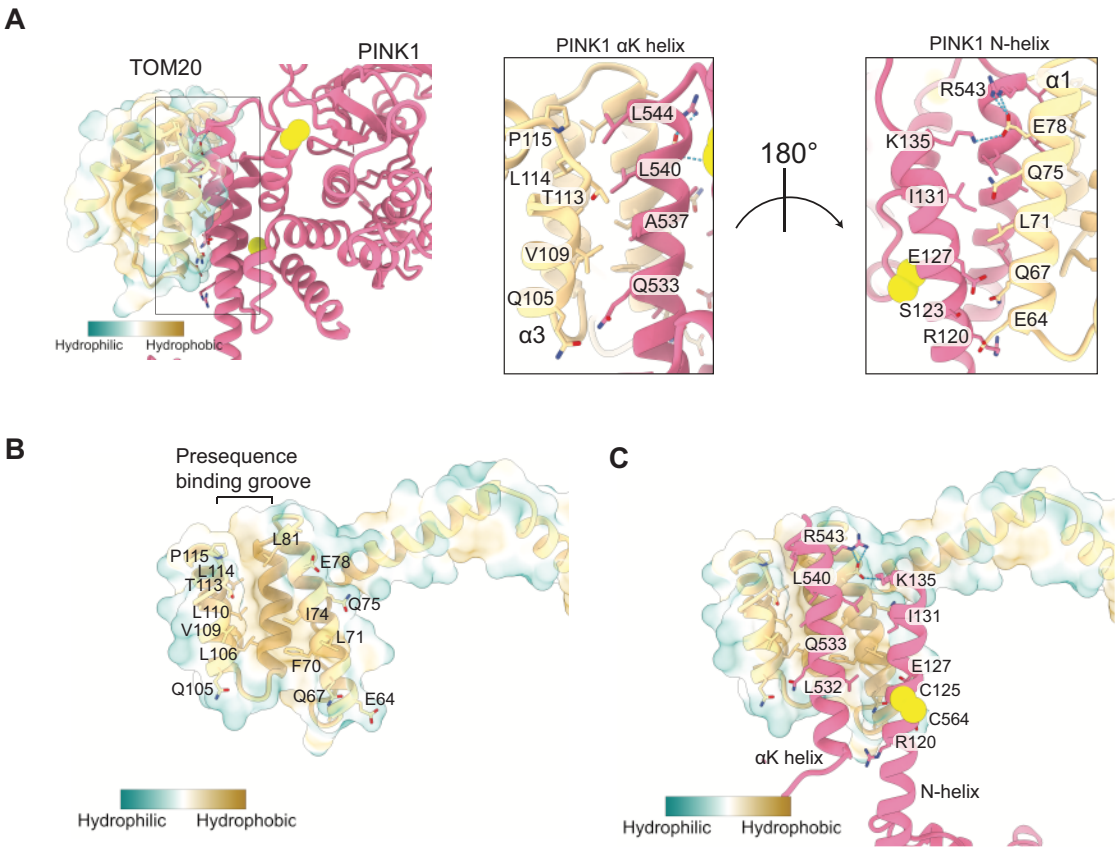

Fig. S12: Interaction of PINK1 with TOM20

(A) PINK1 bound to the cytosolic domain of TOM20. For TOM20, the atomic model is shown within the surface model, colored to depict hydrophobicity. Disulfide bonds are shown as yellow spheres. Insets show closeups of interacting residues of the PINK1 αK helix and the PINK1 N-terminal helix respectively. **(B)** TOM20 as in (A), but without PINK1 and rotated to show the hydrophobic presequence binding groove. **(C)** As in (B) but showing the bound PINK1 αK and N-terminal helices. The sideview function on ChimeraX was used to depict the relevant helices.

Fig. S12.
Interaction of PINK1 with TOM20.

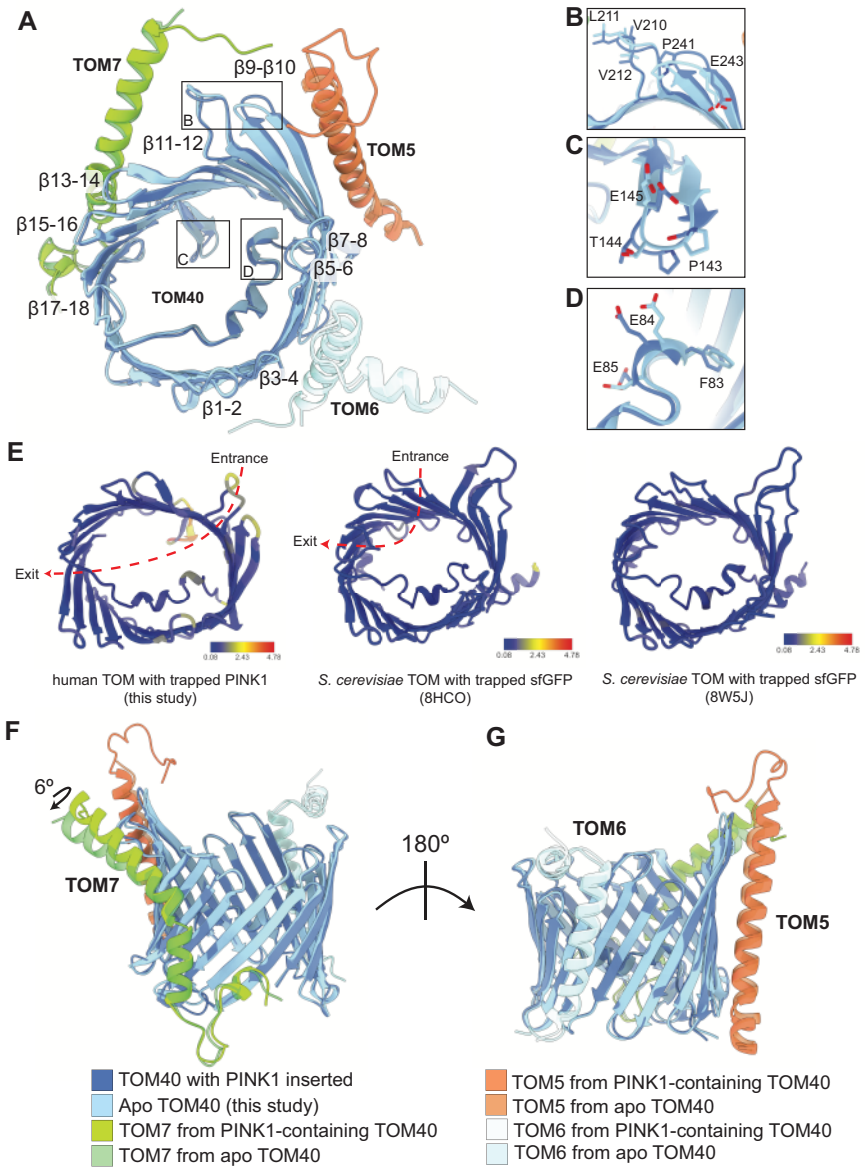

Fig. S13: Comparison of Apo-TOM40 barrel with PINK1-trapped TOM40 barrel.

(A) Apo TOM40 and associated small TOMs superimposed on the proximal PINK1-trapped TOM40 unit from our structure. View is from cytoplasm. **(B)**, **(C)** and **(D)** insets from (A) showing closeup view of alterations in the TOM40 entrance loops, exit loop and N-terminal helix respectively.
(E) PINK1-trapped TOM40 barrel from this study compared with yeast TOM40 barrels containing a trapped sfGFP tagged precursor protein *(51,69)*. The atomic model of the substrate bound TOM40 is coloured according to RMSD after alignment of substrate bound TOM40 to the proximal apo-TOM40.
(F) and **(G)** two rotations of the TOM complexes, as in (A), but viewed from the membrane plane.

Fig. S13.
Comparison of Apo-TOM40 with PINK1-trapped TOM40.

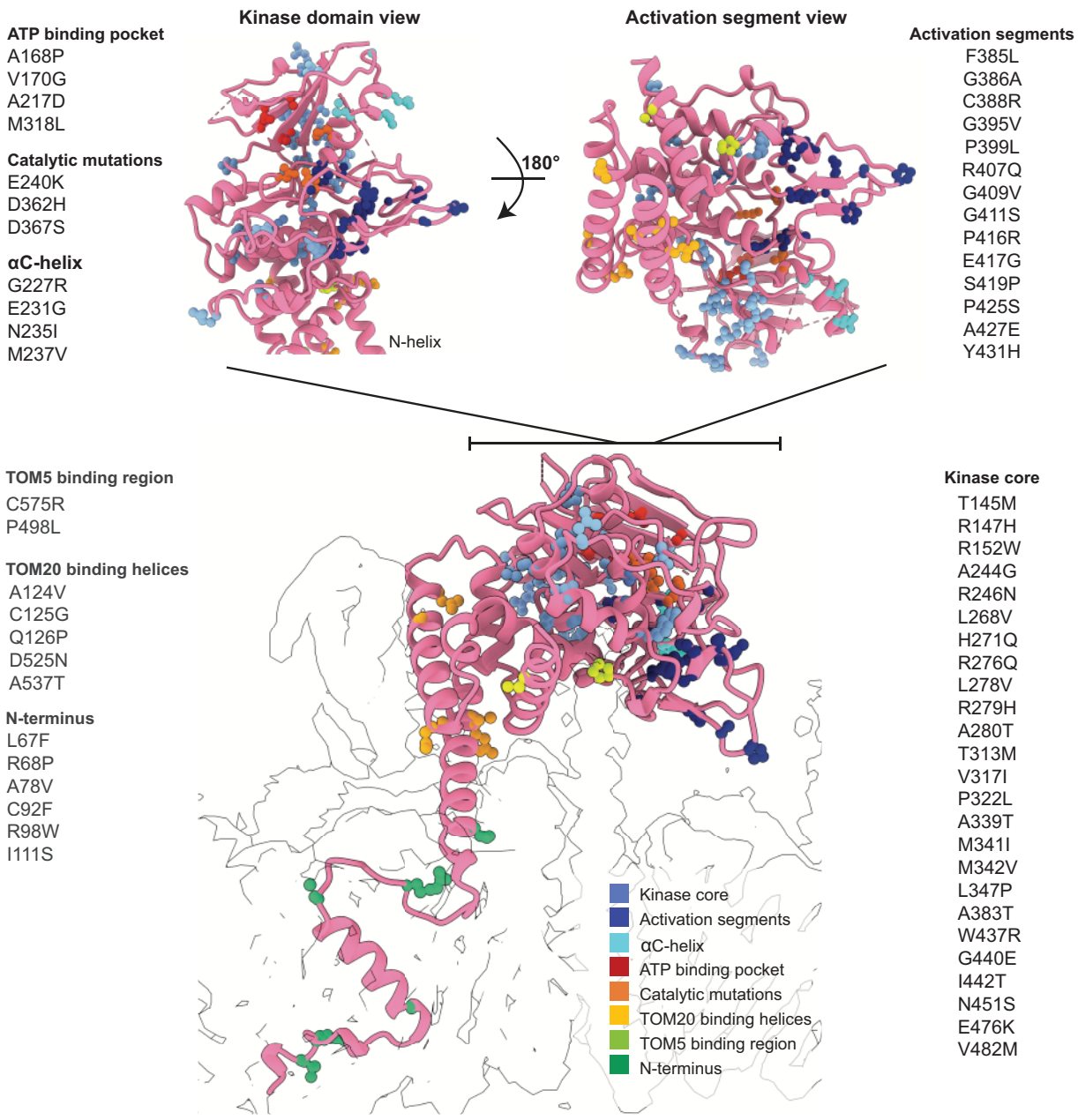

Fig. S14: Missense PINK1 patient mutations that cause early-onset Parkinson's disease

Structure of human PINK1 showing residues mutated in patients with early-onset Parkinson's disease from *(23)*. Mutated residues are shown as coloured spheres. Insets above show a closeup of the kinase domain and a rotation of the kinase domain depicting the activation segments.

Fig. S14.
Missense PINK1 patient mutations that cause early-onset Parkinson's disease.

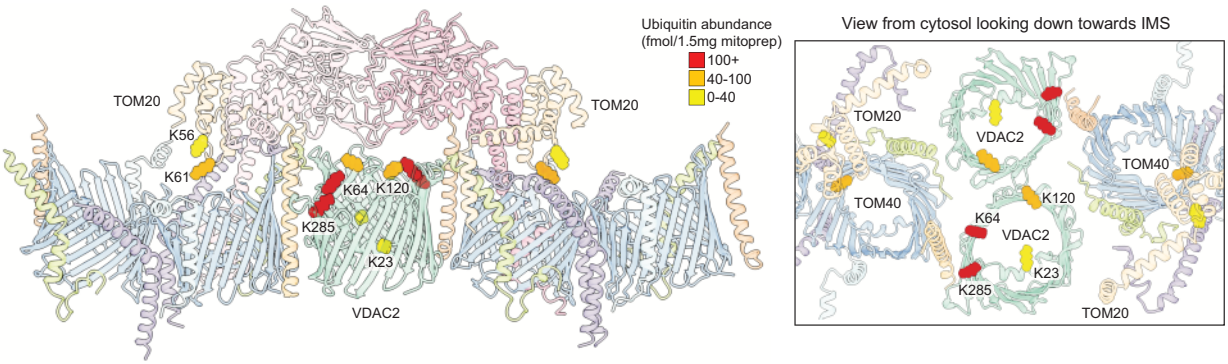

Fig. S15: Parkin-dependent TOM-VDAC ubiquitination sites

Atomic model of the PINK1-TOM-VDAC complex, viewed along the membrane plane, showing Parkin-dependent ubiquitinated lysed residues (coloured spheres), based on published Parkin-dependent ubiquitinomics data *(18)*. Lysines are coloured based on the abundance of Kgg peptide detected (fmol/1.5mg mitoprep) *(18)*. Inset shows closeup of ubiquitinated lysines on VDAC2, with PINK1 removed, as viewed from the cytosol.

Fig. S15.
Parkin-dependent TOM-VDAC ubiquitination sites.

Table S1.

Protein 1	Protein 2	Linked residue protein 1	Linked residue protein 2
PINK1	TIM50	46	284
PINK1	TIM50	44	284
PINK1	TOM40	114	248
PINK1	TOM40	118	240
PINK1	TOM20	137	77
PINK1	TIM17B	24	137
PINK1	TIM17B	24	136
PINK1	TOM7	127	6
TOM40	TIM50	308	334
TOM40	TIM50	328	332
TOM40	TIM50	308	332
TOM40	TIM50	329	334
TOM40	TIM50	309	324
TOM40	TOM20	122	61
TOM40	TOM7	181	19
TOM40	TOM7	180	16
TOM40	TOM5	246	16
TOM40	TOM5	240	17
TOM20	TOM7	67	17
TIM23	TIM50	52	293
TIM23	TIM50	64	294

SDA Inter-protein crosslinked residues for PINK1-TOM-TIM23 core components.

Table S2.

	Overall complex (EMDB-48083) (PDB 9EIH)	SymExp (EMDB-48084) (PDB 9EII)	Long TOM20 (EMDB-48085) (PDB 9EIJ)
Data collection and processing			
Magnification	105,000	-	-
Voltage (kV)	300	-	-
Electron exposure (e–/Å^2)	52.4	-	-
Defocus range (μm)	-0.5 – -2.0	-	-
Pixel size (Å)	0.833	-	-
Symmetry imposed	C1	Expanded (C2)	-
Initial particle images (no.)	5.6 M	-	-
Final particle images (no.)	347 k	791k	165k
Map resolution (Å)	3.1	2.75	3.3
FSC threshold	0.143	0.143	0.143
Map resolution range (Å)	1.8 – 12.8	1.8 – 31	2.6 – 27
Refinement			
Initial model used (PDB code)	7CP9, AF3	7CP9, AF3	7CP9, AF3
Model resolution (Å)	3.0/3.1/3.5	2.7/2.7/3.0	3.2/3.3/3.5
FSC threshold	(0/0.143/0.5)	(0/0.143/0.5)	(0/0.143/0.5)
Model resolution range (Å)	3.0 – 3.9	2.7 – 3.5	3.2 - 3.8
Map sharpening *B* factor (Å^2)	unsharpened	unsharpened	unsharpened
Model composition			
Non-hydrogen atoms	28909	14459	16982
Protein residues	3584	1789	2121
Ligands	17	9	9
B factors (Å^2)	min/max/mean	min/max/mean	min/max/mean
Protein	0.00/276.07/148.41	38.54/248.58/115.90	25.39/296.10/129.71
Ligand	60.88/208.61/133.34	58.42/166.38/105.11	35.17/151.35/108.88
R.m.s. deviations			
Bond lengths (Å)	0.003 (0)	0.002 (0)	0.002 (0)
Bond angles (°)	0.700 (1)	0.673 (0)	0.647 (0)
Validation			
MolProbity score	1.09	1.24	1.17
Clashscore	1.62	1.85	1.92
Poor rotamers (%)	0.77	1.34	0.96
Ramachandran plot			
Favored (%)	96.96	96.76	96.64
Allowed (%)	2.95	3.19	3.31
Disallowed (%)	0.09	0.06	0.05
Model vs. Data			
CC (mask)	0.79	0.85	0.79
CC (box)	0.70	0.82	0.67
CC (peaks)	0.54	0.66	0.52
CC (volume)	0.79	0.84	0.79
Mean CC (ligands)	0.55	0.57	0.58

Cryo-EM data collection, refinement and validation statistics

Table S2.

Cryo-EM data collection, refinement and validation statistics

Data S1. (separate file)
Mass spectrometry analysis of gel bands from Fig 1C.

Data S2. (separate file)
XL-MS analysis of purified complex.